Title

Inhibition of RNA splicing triggers CHMP7 nuclear entry, impacting TDP-43 function and leading to the onset of ALS cellular phenotypes

Journal

Neuron, 112(24)

ISSN

0896-6273

Authors

Al-Azzam, Norah

To, Jenny H

Gautam, Vaishali

et al.

Publication Date

2024-12-01

DOI

10.1016/j.neuron.2024.10.007

Neuron

Article

Inhibition of RNA splicing triggers CHMP7 nuclear entry, impacting TDP-43 function and leading to the onset of ALS cellular phenotypes

Graphical abstract

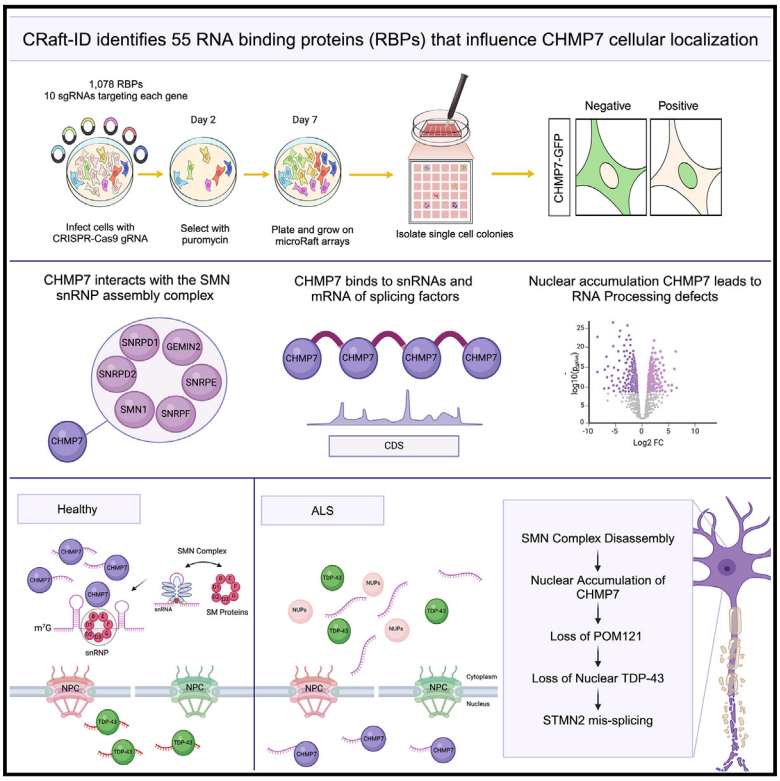

Highlights

- CRaft-ID identifies key regulators of CHMP7 nuclear localization
- CHMP7 interacts with snRNP assembly factors, SM proteins, and Gemin proteins
- CHMP7 binds snRNAs and mRNAs that encode essential splicing factors
- Inhibition of SMN complex triggers CHMP7 nuclear entry, affecting TDP-43 function

Authors

Norah Al-Azzam, Jenny H. To, Vaishali Gautam, ..., Alyssa N. Coyne, Marko Jovanovic, Gene W. Yeo

Correspondence

geneyeo@ucsd.edu

In brief

Al-Azzam et al. reveal that SmD1, a member of the SMN complex, regulates CHMP7 translocation. Reduced SmD1 expression in sporadic ALS leads to CHMP7 nuclear translocation, while overexpression prevents it, highlighting SmD1's role in ALS pathogenesis.

Al-Azzam et al., 2024, Neuron *112*, 1–15
December 18, 2024
https://doi.org/10.1016/j.neuron.2024.10.007

CellPress

Please cite this article in press as: Al-Azzam et al., Inhibition of RNA splicing triggers CHMP7 nuclear entry, impacting TDP-43 function and leading to the onset of ALS cellular phenotypes, Neuron (2024), https://doi.org/10.1016/j.neuron.2024.10.007

Neuron

CellPress
OPEN ACCESS

Article

Inhibition of RNA splicing triggers CHMP7 nuclear entry, impacting TDP-43 function and leading to the onset of ALS cellular phenotypes

Norah Al-Azzam,[1,2,3,4] Jenny H. To,[1,2,3] Vaishali Gautam,[1,2,3] Lena A. Street,[5] Chloe B. Nguyen,[1,2,3] Jack T. Naritomi,[1,2,3] Dylan C. Lam,[1,3,6] Assael A. Madrigal,[1,7] Benjamin Lee,[1,2,3] Wenhao Jin,[6] Anthony Avina,[1,2,3] Orel Mizrahi,[1,2,3] Jasmine R. Mueller,[1,2,3] Willard Ford,[1,2,3] Cara R. Schiavon,[8,9] Elena Rebollo,[8,9] Anthony Q. Vu,[1,2,3] Steven M. Blue,[1,2,3] Yashwin L. Madakamutil,[1,2,3] Uri Manor,[8,9] Jeffrey D. Rothstein,[10,11] Alyssa N. Coyne,[10,11] Marko Jovanovic,[5] and Gene W. Yeo[1,2,3,6,12,*]

[1]Department of Cellular and Molecular Medicine, University of California San Diego, La Jolla, CA, USA
[2]Sanford Stem Cell Institute Innovation Center and Stem Cell Program, University of California San Diego, La Jolla, CA, USA
[3]Institute for Genomic Medicine, University of California San Diego, La Jolla, CA, USA
[4]Neurosciences Graduate Program, University of California San Diego, San Diego, CA, USA
[5]Department of Biological Sciences, Columbia University, New York, NY, USA
[6]Sanford Laboratories for Innovative Medicines, San Diego, CA, USA
[7]Department of Biological Sciences Graduate Program, University of California San Diego, La Jolla, CA, USA
[8]Department of Cell and Developmental Biology, University of California San Diego, La Jolla, CA, USA
[9]Waitt Advanced Biophotonics Center, Salk Institute for Biological Studies, 10010 N. Torrey Pines Road, La Jolla, CA 92037, USA
[10]Brain Science Institute, Johns Hopkins University School of Medicine, Baltimore, MD 21205, USA
[11]Department of Neurology, Johns Hopkins University School of Medicine, Baltimore, MD 21205, USA
[12]Lead contact
*Correspondence: geneyeo@ucsd.edu
https://doi.org/10.1016/j.neuron.2024.10.007

SUMMARY

Amyotrophic lateral sclerosis (ALS) is linked to the reduction of certain nucleoporins in neurons. Increased nuclear localization of charged multivesicular body protein 7 (CHMP7), a protein involved in nuclear pore surveillance, has been identified as a key factor damaging nuclear pores and disrupting transport. Using CRISPR-based microRaft, followed by gRNA identification (CRaft-ID), we discovered 55 RNA-binding proteins (RBPs) that influence CHMP7 localization, including SmD1, a survival of motor neuron (SMN) complex component. Immunoprecipitation-mass spectrometry (IP-MS) and enhanced crosslinking and immunoprecipitation (CLIP) analyses revealed CHMP7's interactions with SmD1, small nuclear RNAs, and splicing factor mRNAs in motor neurons (MNs). ALS induced pluripotent stem cell (iPSC)-MNs show reduced SmD1 expression, and inhibiting SmD1/SMN complex increased CHMP7 nuclear localization. Crucially, overexpressing SmD1 in ALS iPSC-MNs restored CHMP7's cytoplasmic localization and corrected STMN2 splicing. Our findings suggest that early ALS pathogenesis is driven by SMN complex dysregulation.

INTRODUCTION

Amyotrophic lateral sclerosis (ALS) is a severe neurodegenerative disease characterized by the progressive degeneration of both upper and lower motor neurons (MNs), resulting in the loss of motor function, respiratory failure, and ultimately death.[1,2] While the etiology of ALS remains multifaceted and poorly understood, recent research has shed light on a new aspect of its pathogenesis.

Nucleoporins, essential components of the nuclear pore complex (NPC), have been observed to be diminished in up to 90% of sporadic ALS (sALS) cases.[3–6] Studies have identified that the abnormal nuclear localization of charged multivesicular body protein 7 (CHMP7), a component of the endosomal sorting complexes required for transport endosomal III (ESCRT-III) degradation pathway, causes NPC injury.[4] This intriguing discovery highlights the critical roles of CHMP7 and the NPC in ALS pathogenesis, prompting further investigation into the regulatory mechanisms governing CHMP7 localization. In this study, we elucidate the molecular pathways linking nucleoporin deficiency to aberrant CHMP7 nuclear localization by identifying survival of MN (SMN) complex dysfunction as an unexpected contributor to the onset and progression of sALS.

The SMN protein complex is an essential assembly component in small nuclear ribonucleoprotein particle (snRNP) formation.[7] Its primary function is to facilitate the efficient and specific

Please cite this article in press as: Al-Azzam et al., Inhibition of RNA splicing triggers CHMP7 nuclear entry, impacting TDP-43 function and leading to the onset of ALS cellular phenotypes, Neuron (2024), https://doi.org/10.1016/j.neuron.2024.10.007

binding of the heteroheptameric Sm complex to a conserved binding site found on the spliceosomal U1, U2, U4, and U5 small nuclear RNAs (snRNAs).[8–11] Sm proteins are gradually assembled together with snRNA in the cytoplasm,[12] resulting in the creation of functional snRNPs, which are essential for the splicing of pre-messenger RNA (pre-mRNA) in the nucleus of eukaryotic cells. SmD1, along with six other snRNP proteins (SmB, SmD2, SmD3, SmE, SmF, and SmG), forms a heptameric ring structure crucial for the assembly of snRNPs, which surround U-rich snRNAs and play a pivotal role in pre-mRNA splicing.[13] SmD1 depletion can affect Sm protein-protein interaction, which can interfere with complex formation with SMN and decrease the levels of U1, U2, U4, and U5 snRNPs.[14,15] These findings underscore the essential role of Sm proteins in splicing, snRNA maturation, and stability.[16]

Dysregulation or mutations in the SMN complex have been associated with various neurodegenerative diseases, such as spinal muscular atrophy (SMA), underscoring its significance in both development and disease.[17,18] Recent investigations have further highlighted its relevance in the pathogenesis of ALS, especially in sporadic cases (sALS).[19] TDP-43 knockout mice and mutant SOD1 mice also exhibit Gemin deficiency.[20,21] Furthermore, Gemin deficiency exacerbates cellular stress and degeneration in ALS.[20,22] Building on this context, through an image-based CRISPR screen using the CRISPR-based microRaft followed by guide RNA identification (CRaft-ID) workflow,[23] we have identified RNA processing proteins, particularly those integrated into the SMN complex, as critical regulators of CHMP7 subcellular localization. Confirming our findings, depletion of SMN complex components results in nuclear localization of CHMP7. As previously established, Sm complex proteins and CHMP7 utilize the exportin protein XPO1 for active transport from the nucleus to the cytoplasm.[24,25] We demonstrate that CHMP7 interacts with SMN complex proteins in MNs. This interaction is mirrored at the RNA level, with CHMP7 binding to snRNAs and mRNAs encoding constitutive and alternative splicing (AS) factors. We observe reduced expression of SmD1, a component of the SMN complex in sALS induced pluripotent stem cell (iPSC)-derived MNs. As CHMP7 nuclear localization causes NPC injury,[4] which leads to loss of nuclear TDP-43 and reduced levels of STMN2 protein,[26–28] we show that restoration of SmD1 levels in sALS iPSC-MNs returns CHMP7 to the cytoplasm and corrects regulation of STMN2 protein. Collectively, our findings suggest the existence of an early pathway involving dysregulation of the SMN complex, which drives the initial stages of sALS pathogenesis.

RESULTS

Image-based genome-wide CRISPR screen technology identifies modulators of CHMP7 nuclear localization

To identify genes that modulate the subcellular localization of CHMP7, we employed the CRaft-ID imaging-based screening and analysis workflow to evaluate a lentiviral library with >12,000 single-guide RNAs (sgRNAs) targeting over 1,000 annotated RNA-binding proteins (RBPs).[23] A HeLa cell line expressing endogenously GFP-tagged CHMP7 was transduced with the lentivirus-packaged library at low multiplicity of infection and sparsely seeded on Cell Microsystems CytoSort arrays, each containing 40,000 "microRafts" (100 × 100 μm). A total of 12 microRaft arrays seeded at 20% cell occupancy were imaged and 84 individual microRafts containing cells with nuclear localized CHMP7-GFP were isolated using the CellRaft AIR System (Figure 1A). Cells from candidate rafts were assigned a unique barcode by targeted PCR of the sgRNA insert and pooled for NGS sequencing after gel extraction and cleanup (Figures 1A and S1A–S1C). For reference, we picked a representative library containing the six pooled rafts which we ran on the Agilent Tapestation for gel extraction to isolate 220–250 bp DNA (Figure S1C). The final DNA library was subjected to sequencing on the Miseq (Illumina) platform and the identities of the sgRNAs were extracted by the CRaft-ID software package (Figure 1A). The model-based analysis of genome-wide CRISPR-Cas9 knockout (MAGeCK) algorithm[29] was used to identify statistically significantly enriched sgRNAs. We successfully identified 73 guides (from 84 rafts) representing 55 candidate genes (Figure 1B) of which some are involved in RNA processing steps such as in RNA splicing (SNRPD1/SmD1, NOVA2) and mRNA translation (EIF2AK2, EIF4G2, and EIF2AK4) (Figures 1C and S1D).

RNA processing plays a pivotal role in governing the cellular localization of CHMP7

Of the 55 genes, we prioritized 23 candidates that had appeared at least twice in the screen and have roles in RNA splicing, implications in ALS biology and RNA export/transport. We utilized XPO1 as a positive control that is known to facilitate the active export of CHMP7 from the nucleus.[25] To confirm the CRaft-ID results, we depleted each candidate gene in wild-type (WT) HeLa cells, each with two different small interfering RNAs (siRNAs). Where antibodies were available, we confirmed a minimum of 80% protein reduction through western blot analysis (Figures S2A and S2B). Knockdown (KD) of eight genes (NOVA2, DDX43, TUBA1B, FAM120C, SNRPD1, DHX8, XPO4, and XPO7) had minimal or no effect on CHMP7 protein levels, indicating that translocation of CHMP7 was not simply due to overall changes in CHMP7 expression (Figure S2C). Three of these candidates, XPO7, XPO4, and DHX8, are export factors known to mediate the nuclear export of proteins and RNA.[30–32] Using immunofluorescence, we assessed cytoplasmic and nuclear intensity of endogenous CHMP7 protein HeLa cells following the confirmation of protein depletion (Figures 2A–2D and S2B). A notable increase in CHMP7 nuclear localization was observed for our candidate RNA processing proteins (Figure 2E). Depletion of SmD1 encoded by the SNRPD1 gene caused the highest increase in CHMP7 nuclear localization, akin to the positive control XPO1 (Figure S2D). SmD1 is a component of the Sm-class snRNPs and is critical for the assembly of U4 snRNP,[33] but it has no prior reported interactions with CHMP7.

CHMP7 interacts with the SMN snRNP assembly complex in iPSC-MNs

To investigate whether CHMP7 protein interacts with our candidate proteins in an RNA-dependent manner, we immunoprecipitated (IP) endogenous CHMP7 protein complexes from

Please cite this article in press as: Al-Azzam et al., Inhibition of RNA splicing triggers CHMP7 nuclear entry, impacting TDP-43 function and leading to the onset of ALS cellular phenotypes, Neuron (2024), https://doi.org/10.1016/j.neuron.2024.10.007

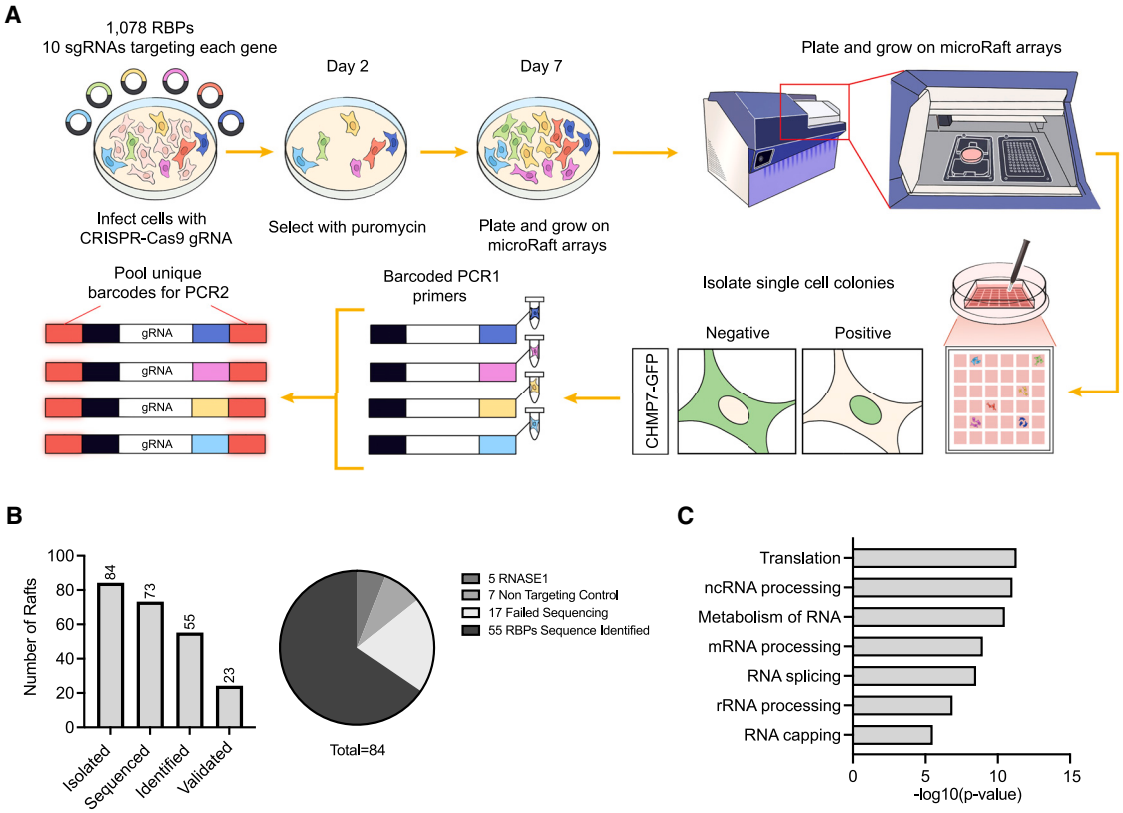

Figure 1. Image-based genome-wide CRISPR screen technologies identifies modulators of CHMP7 nuclear localization

(A) Schematic of the CRaft-ID experiment. A CRISPR-Cas9 gRNA library was generated from an array of sgRNA oligonucleotides cloned into the lentiCRISPR v2 backbone. HeLa cells expressing GFP-CHMP7 were infected at low multiplicity of infection (MOI 0.15) and cultured in bulk for 7 days after selection, allowing lethal guides to drop out of the pool. A bulk infection of cells with a gRNA library targeting over 1,000 annotated proteins (>12,000 sgRNAs) was performed, followed by single cell plating on 12 microRaft arrays to screen genetic knockout clones for mislocalization of CHMP7. Positive candidates, where GFP is in the nucleus and co-localizing with nuclear staining by DAPI, were selected. To sequence the sgRNA associated with CHMP7 mislocalization to the nucleus, we isolated target colonies adhered to microRafts from the array. A motorized microneedle, fitted over the microscope objective, was actuated to pierce the polydimethylsiloxane (PDMS) microarray substrate and dislodge individual magnetic microRafts from the array. Released microRafts and their cargo were collected with a magnetic wand into a strip tube containing a lysis buffer for a targeted two-step PCR with in-line barcodes, followed by high-throughput sequencing.
(B) Bar chart showing the total number of rafts picked (84), sequenced (73 with successfully obtained PCR products), and identified (55 using CRaft-ID) and proteins confirmed by siRNA depletion (23). The pie chart represents the distribution of sgRNAs identified from the 84 rafts.
(C) GO analysis of the 55 candidate genes identified in the screen compared with the background of genes targeted in the CRISPR screen.

iPSC-derived differentiated MNs (iPSC-MNs) at day 28 with or without RNase treatment, followed by mass spectrometry analysis (Figure 3A). We identified 379 enriched proteins in CHMP7-IP samples relative to an IgG control in the untreated condition (p value < 0.01 and greater than 2-fold difference; Figure 3B; Table S1). CRaft-ID candidates SNRPD1/SmD1, EIF2AK2, RRP1, and GAR1 were identified as interactors of CHMP7 in the untreated samples, with two additional candidates EIF4G2 and XPO7 found as enriched under a less stringent p value cutoff of 0.05 (Figure 3B; Table S1). Following treatment with RNase, we observed a ~75% reduction in the total number of enriched interactions, suggesting that CHMP7's protein-protein interactome is largely RNA-mediated (Figure 3C). In untreated conditions, the interacting proteins displayed an enrichment for RNA processing factors, such as RNA transport, splicing modulators, translation regulatory proteins, snRNPs, and RNA helicases (Figure 3D). In RNase-treated samples, this network shifted toward the SUMOylation of DNA methylation, glycogen synthesis and degradation, actin cytoskeleton organization, and glycogen metabolic process unrelated to RNA metabolism (Figure 3E). Despite CHMP7 being predominantly cytoplasmic, we identified both cytoplasmic and nuclear proteins, as well as those known to shuttle between the nucleus and cytoplasm, suggesting a functional role for CHMP7 in both cellular compartments consistent with prior reports.[34–38] Cluster analysis was performed to characterize molecular functions for the CHMP7 interacting proteins in untreated samples. Our analysis identified several candidates within the SMN complex, which itself is critical for biogenesis of spliceosomal snRNPs,[16,39] as well as within mRNA transport and RNA processing machineries (Figure 3F). Upon closer examination of CHMP7 RNA-mediated interactions, we observed its close association with Gemin proteins and SmD proteins, all integral components of the snRNP assembly pathway (Figure 3G). Indeed, our analysis revealed a larger

Please cite this article in press as: Al-Azzam et al., Inhibition of RNA splicing triggers CHMP7 nuclear entry, impacting TDP-43 function and leading to the onset of ALS cellular phenotypes, Neuron (2024), https://doi.org/10.1016/j.neuron.2024.10.007

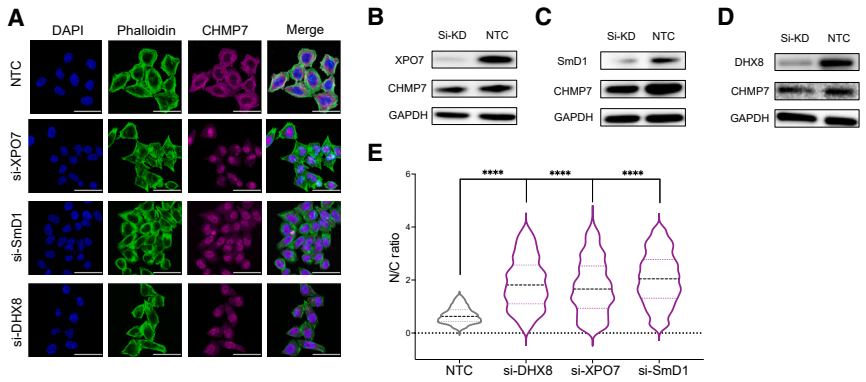

Figure 2. RNA processing plays a pivotal role in governing the cellular localization of CHMP7

(A) Representative images of proteins XPO7, DHX8, and SmD1 depleted by siRNAs in HeLa cells. Immunofluorescent analysis of DAPI (blue), phalloidin (actin filaments, green), and CHMP7 (magenta). Scale bars, 50 μm.

(B–D) Western blot analysis of XPO7, SmD1, and DHX8 in cells treated with targeting siRNAs, alongside NTCs.

(E) Quantification of image intensity of cytoplasmic (C) and nuclear (N) CHMP7 in HeLa cells when XPO7, DHX8, and SmD1 are targeted by siRNA, compared with NTC, represented by the y axis label as N/C ratio. Data are presented as mean ± SD of three independent experiments (n = 3 wells, ∼800 cells total). Statistical significance analyzed by Student's t test, ****$p < 0.0001$.

number of interactions with the components of the SMN complex compared with nucleoporins (Nups) (Figure 3G). Given that the biogenesis of spliceosomal snRNPs involves multiple steps in both nuclear and cytoplasmic phases, our results suggest that CHMP7 and SMN could be involved in a coordinated regulation of these RNA-related processes.

CHMP7 binds to snRNAs and mRNA of splicing factors in iPSC-MNs

Given that 57% of CHMP7's interacting proteins are annotated RBPs, we reasoned that CHMP7 itself may have RNA-binding capabilities. We employed our deep-learning RBP classifier HydRA[40] to identify potential RNA-binding domains (RBDs) and low-complexity regions (LCRs) across the CHMP7 protein sequence. HydRA's occlusion map analysis indicates that CHMP7 has predicted RNA-binding regions at 126–174 and 206–226 amino acids (aa) ($p < 0.05$) and at 141–166 aa ($p < 0.001$), proximal to the N-terminal of the Snf7 domain (Figure 4A). We conducted enhanced crosslinking and immunoprecipitation (eCLIP) analysis on CHMP7 in iPSC-MNs after IP pull-down confirmation (Figure S3A).[41] Both CHMP7 IP replicates passed statistical thresholds to maximize the number of hits (Figure S3B) as specified by the Skipper computational workflow,[42] and had high concordance between replicates (Figure S3C). After processing all IPs separately, we selected reproducibly enriched windows for both transcriptomic regions and repetitive elements, satisfying a 20% false discovery rate (FDR) cutoff (Figure S3D).We found that CHMP7 interacts with transcripts from protein-coding genes (Figure 4B; Table S2), binding primarily to CDS and 5′ untranslated regions (5′ UTRs) (Figure 4C), suggesting that CHMP7 interacts with mature mRNAs in the cytoplasm, reminiscent of other RBPs that had CDS preferences analyzed by ENCODE3 (Figure 4D).[43] We assessed the motifs enriched within CHMP7 enriched regions and found two statistically significant motifs, namely CGG ($p < 10^{-53}$) and UGG ($p < 10^{-44}$) (Figure S3E).

To characterize the genes enriched for CHMP7 binding, we conducted a Gene Ontology (GO) enrichment analysis, revealing significantly enriched terms "axon extension," "transport along microtubule," "synapse assembly," "splicesomal complex," "U2 and U5 SNRNP," and "dynein complex binding" (Figure 4E). To illustrate, we discovered CHMP7 binding to exonic regions of mRNAs encoding splicing factors SF1 and PRPF40 (Figure S3F). These genes encode integral protein constituents of snRNPs or are actively engaged in splicing through U1 or U2 snRNPs.[44] We also observed binding to SNRNP70 which enables U1 snRNA binding activity (Figure S3F). CHMP7 also exhibited enriched binding to noncoding RNAs such as microRNAs (miRNAs), long noncoding RNAs (lncRNAs), and snRNAs such as RNU1, RNU2, and RN7SK (Figures 4B, 4F, and 4G). This direct binding establishes connections to snRNA complex formation or regulation at the RNA level, complementing our protein-protein interaction results. In summary, CHMP7 appears to interact with the RNAs of splicing factors and snRNAs involved in snRNP formation and splicing.

Impaired nuclear export of CHMP7 has consequences on RNA processing

To investigate the potential impact of CHMP7's subcellular localization on RNA metabolism, we obtained two mutants of CHMP7 from a previous study done on nuclear envelope reformation and modified the plasmids with EF-1α promoter.[45] Predictions suggested that two nuclear export sequences (NESs) in helices 5 and 6[25,46] regulate CHMP7's interaction with XPO1. To generate nuclear localized CHMP7 cell models, we depleted CHMP7 in HeLa cells using siRNAs and transfected GFP-tagged CHMP7 mutants: GFP-CHMP7, helix 6 (GFP-CHMP7^{NES2-}) or helix 5 and helix 6 (GFP-CHMP7$^{NES1-\&NES2-}$). As anticipated, while observing nuclear accumulation of CHMP7 with the GFP-CHMP7^{NES2-} mutant, the GFP-CHMP7$^{NES1-\&NES2}$ mutant demonstrated clustering at the nuclear envelope and peripheral ER instead as previously shown (Figure 5A).[45] We next performed RNA sequencing (RNA-seq) analysis on cells transfected with GFP-CHMP7^{NES2-} relative to control GFP-CHMP7 to identify genes that are differentially expressed because of CHMP7 localization (Figure 5B; Table S3). GO analysis of genes downregulated by CHMP7 nuclear localization were enriched for cytoplasmic translation, RNA splicing, mitochondrial translation, spliceosomal complex assembly, and nuclear export. Upregulated genes were involved in metabolic processing (Figure 5C). Using rMATS turbo v4.2.0, we also identified a total of 774 AS events with an FDR ≤ 0.05 between GFP-CHMP7^{NES2-} vs.

Please cite this article in press as: Al-Azzam et al., Inhibition of RNA splicing triggers CHMP7 nuclear entry, impacting TDP-43 function and leading to the onset of ALS cellular phenotypes, Neuron (2024), https://doi.org/10.1016/j.neuron.2024.10.007

CellPress
OPEN ACCESS

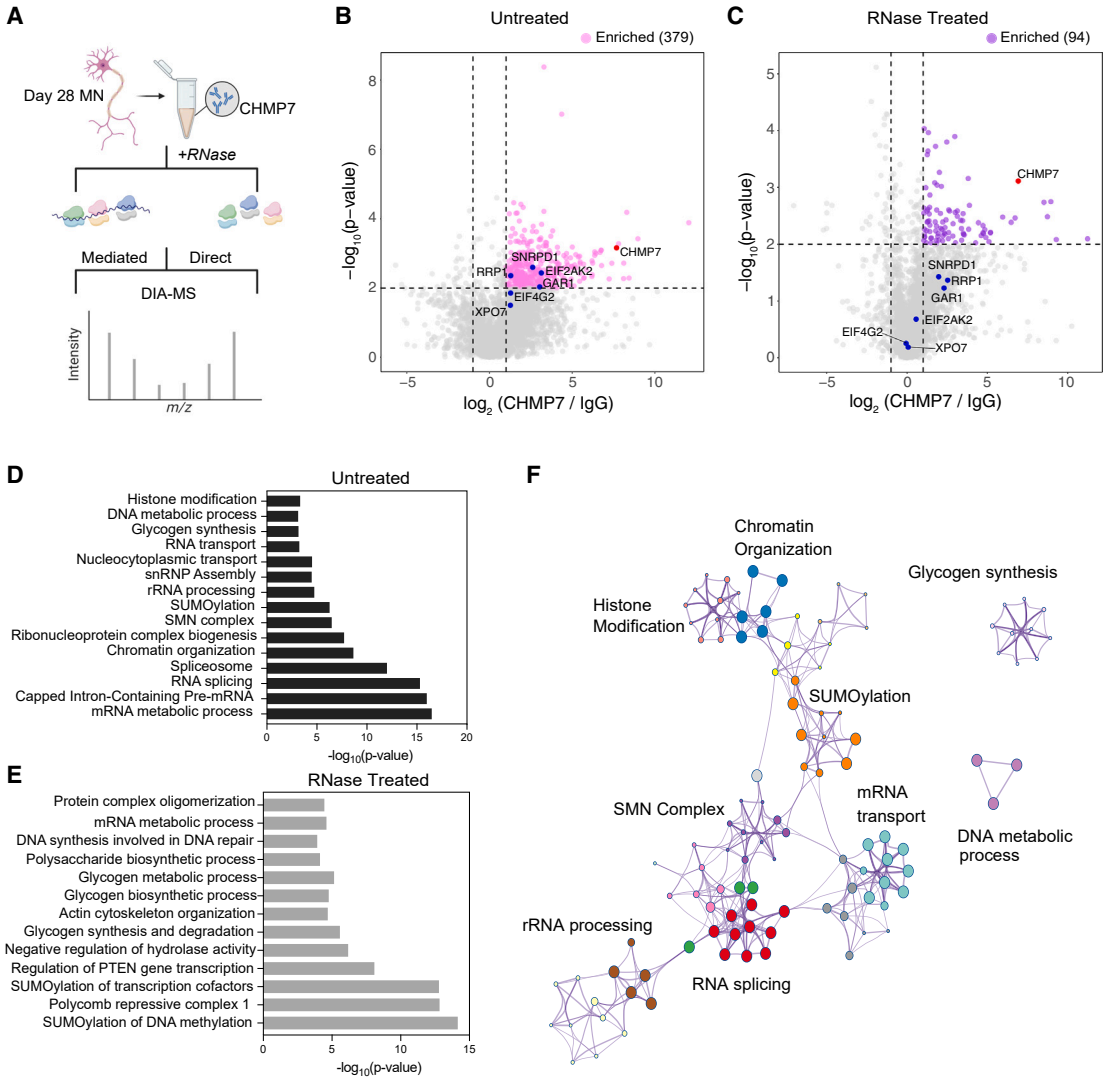

(legend on next page)

Please cite this article in press as: Al-Azzam et al., Inhibition of RNA splicing triggers CHMP7 nuclear entry, impacting TDP-43 function and leading to the onset of ALS cellular phenotypes, Neuron (2024), https://doi.org/10.1016/j.neuron.2024.10.007

GFP-CHMP7, of which 378 events exhibited a change in percent-spliced-in (Ψ) value of 10% or more (Figure 5D; Table S4). An analysis of the genes with AS events highlighted "mRNA splicing" and "chromatin organization" as the most highly represented GO terms (Figure S4A). This indicates that nuclear retained CHMP7 impacts crucial cellular processes related to RNA metabolism.

Changes in both RNA-binding profile and protein interactions in sALS iPSC-MNs

Next, we investigated whether there are differences in the protein interactors of CHMP7 in iPSC-MNs from sALS lines (Figure S4B). We performed the IP of CHMP7 and evaluated it for interacting SMN complex proteins by western blot analysis. We observed a slight reduction in SmD1 interaction with CHMP7 in sALS lines (Figure S4B). This observation led us to exploring the transcriptome-wide CHMP7 protein-RNA landscape in ALS iPSC models, where CHMP7 is aberrantly localized within the nucleus. To accomplish this, we generated MNs from iPSC lines from two healthy controls, two familial ALS patients with G4C2 repeat expansions in the C9ORF72 locus and two sALS patients. To identify CHMP7 RNA-binding in ALS, we conducted eCLIP analysis[41] on each cell line using an antibody recognizing endogenous CHMP7 protein and quantified the number of enriched transcriptomic regions bound by the protein. In healthy control iPSC-MNs, we found a substantial enrichment in CDS and exons as we previously observed (Figures 4C and 6A). However, in both C9orf72 and sALS iPSC-MNs, we discovered a 3-fold reduction in CHMP7 binding to CDS, coupled with an increase in binding to intronic regions (Figures 6B and 6C). Upon performing cluster analysis, we observed that CHMP7 binding in C9orf72 and sALS iPSC-MNs clustered with RBPs that typically interacted with intronic regions and splice sites (Figure 6D). By averaging across all transcripts using metadensity plots,[47] we detected prevalent intronic region binding, most likely due to CHMP7's nuclear localization in both C9orf72 and sALS iPSC-MNs (Figure 6E). Concurrently, we saw a reduction in 5′ UTR binding in sALS iPSC-MNs compared with control lines (Figure 6F). Next, we analyzed AS events from sALS and C9orf72 iPSC-MN compared with control RNA-seq datasets.[48] At a FDR $\leq$ 0.01, we identified 1,038 AS events that exhibited a change of Ψ of more than 10% between ALS and control (Figure S4C). We then tested the hypothesis that there was an association between CHMP7 binding and AS-containing genes. Out of 49 genes with intronic CHMP7-binding sites, 10 exhibited differential AS events. Among the 15,922 non-CHMP7-bound genes, 1,028 had significant events, confirming a statistically significant association ($p < 0.00007$; chi-squared statistic of 15.69; Figure S4C; Table S5). The 49 genes with enriched intronic binding were associated with GO terms "regulation of mRNA metabolic process," "positive regulation of ERK1 and ERK2 cascade," "regulation of cellular catabolic process," "FCERI mediated MAPK activation," and "apoptosis" (Figure S4D). Our findings indicate that the abnormal nuclear localization of CHMP7 in C9orf72 and sALS iPSC-MNs contributes to its increased interactions within pre-mRNA intronic regions, likely affecting AS and other RNA processing events. Consequently, this aberrant localization leads to decreased interactions with mature mRNAs.

Overexpression of SmD1 is sufficient to restore subcellular distribution of CHMP7 in sALS iPSC-MNs

Our experiments demonstrated that depletion of SmD1 led to abnormal nuclear localization of CHMP7 in HeLa cells (Figures 2A and 2E). Previous studies have demonstrated that SmD1 depletion blocks splicing at the initial step, resulting in decreased levels of U1, U2, U4, and U5.[14] Given these results, we investigated whether reducing SmD1 levels would induce CHMP7 nuclear localization. After nucleofection with SmD1-targeting siRNA in control iPSC-MNs, we observed increases in nuclear intensity of CHMP7 compared with non-targeting-control (NTC) (Figures 7A and 7B). It has been described that the increased nuclear localization of CHMP7 takes place as an early event in ALS, occurring prior to the manifestation of NPC injury.[49] Therefore, we determined whether SmD1 depletion could initiate NPC injury, presumably following CHMP7 nuclear localization in control iPSC-MNs. We observed reductions in POM121 and Nup133 upon SmD1 protein depletion (Figures S5A and S5B). We next quantified the nuclear intensity of TDP-43 and observed a reduction in TDP-43 immunoreactivity upon SmD1 KD compared with NTC (Figures 7A and 7C). Therefore, we conclude that reduction of SmD1 in iPSC-MNs is sufficient to trigger NPC alterations that have previously been demonstrated to follow aberrant CHMP7 nuclear localization.[4] This overall loss of Nups is thought to impact nuclear transport, disrupt the function of Ran, and result in the loss of TDP-43 nuclear localization and aggregation in the cytoplasm.[50,51]

To assess the functional consequences of altered TDP-43 distribution, we probed for changes in STMN2 cryptic exon splicing, which was found to be a prominent feature of ALS in patients with TDP-43 pathology.[27,28,52] We performed quantitative reverse transcription polymerase chain reaction (RT-qPCR) analysis to quantify full-length and truncated STMN2 mRNA species in the

Figure 3. CHMP7 interacts with SMN complex proteins responsible for snRNP assembly in iPSC-MNs

(A) Schematic of IP-MS workflow to identify CHMP7 protein-protein interactions with or without RNase treatment.

(B and C) Volcano plots showing proteins significantly enriched in untreated or RNase-treated CHMP7 IPs compared with IgG IPs. The x axis shows $\log_2$ fold changes between CHMP7 IP to IgG, and the y axis shows $-\log_{10} p$ values (unpaired Student's t test). Proteins with p values < 0.01 and fold change > 2 are labeled as interactors.

(D and E) GO terms that were enriched for the protein interactors in untreated or RNase-treated samples. The $-\log_{10}$ (p value) depicting the statistical significance of enrichment is plotted for each GO term. Background of all the proteins in IPs was implemented in the GO term analysis. A list of enriched interactors can be found in Table S1.

(F) Network analysis was performed for CHMP7 interactors across all GO term pathways using the Molecular Complex Detection (MCODE) algorithm to identify densely connected protein neighborhoods in the network. The biological roles of each component are annotated.

(G) CHMP7 RNA-mediated interactors associate with snRNP assembly proteins (SmD1–SmD3), GEM, and nuclear pore complex proteins. Nodes are colored based on k-means clustering and edge confidence; high (0.700), highest (0.900), and medium (0.400) from String.

Please cite this article in press as: Al-Azzam et al., Inhibition of RNA splicing triggers CHMP7 nuclear entry, impacting TDP-43 function and leading to the onset of ALS cellular phenotypes, Neuron (2024), https://doi.org/10.1016/j.neuron.2024.10.007

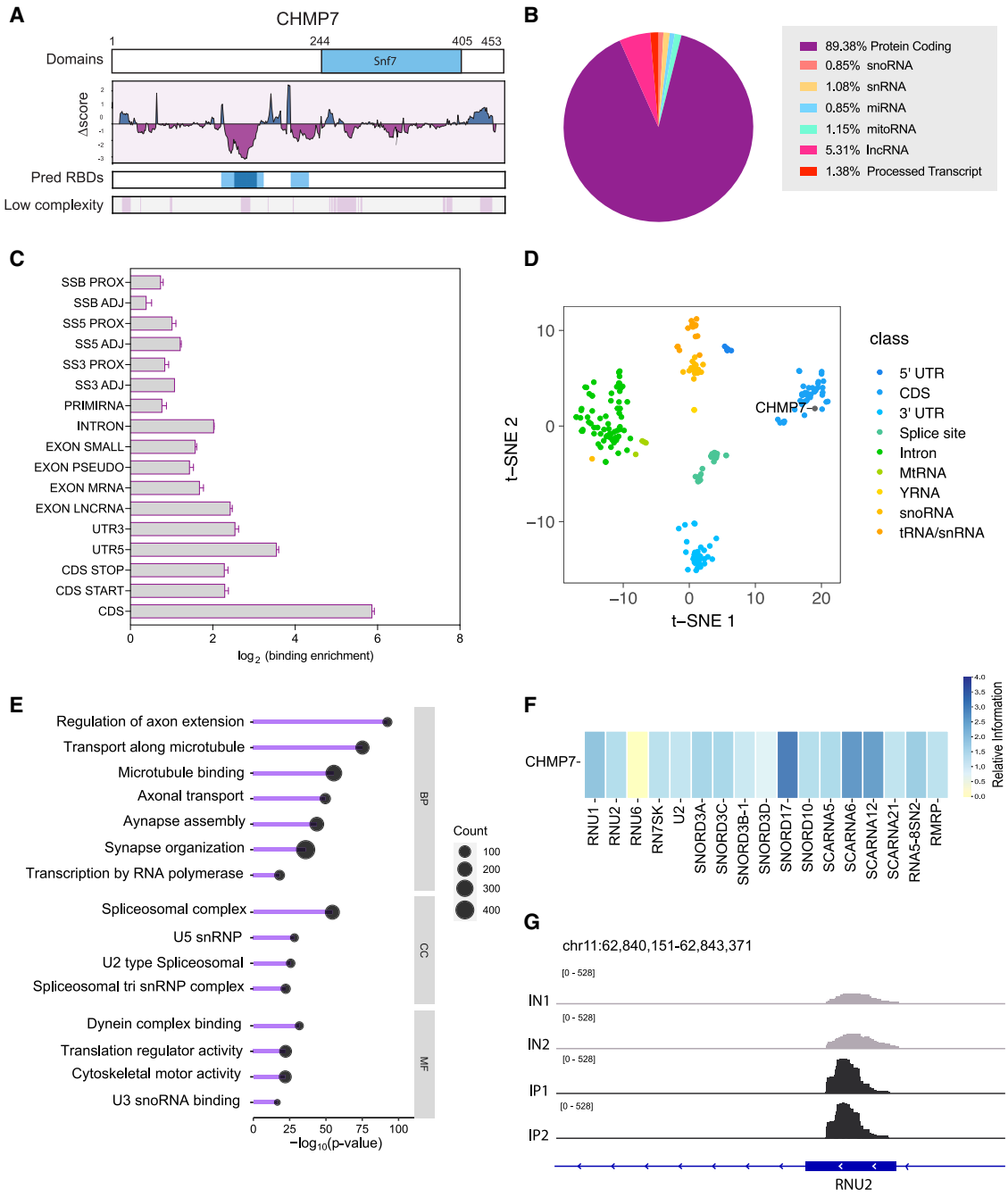

Figure 4. CHMP7 binds RNA, specifically RNA processing targets, in iPSC-MNs

(A) HydRA analysis of CHMP7 protein, with annotations for low complexity regions, and high ΔAS scores representing regions that occlusion analysis indicated to be predicted RBDs.

(B) Pie chart of genomic features represented in enriched windows in CHMP7 eCLIP data from day 28 iPSC-MNs.

(C) Bar plot of gene features of CHMP7 eCLIP-binding enrichment (fold change) normalized to size-matched input control in day 28 iPSC-MNs. The data are presented as the mean ± SD. Skipper analysis was used to compute these enrichments (Table S2).

(D) Comparison of CHMP7 eCLIP with ENCODE3 eCLIP data, clustered by binding preferences to genic features.

(E) Statistically significantly enriched GO terms for CHMP7 RNA targets.

(F) Heatmap indicating relative information for small nucleolar RNA (snoRNA) and snRNA elements with CHMP7 binding.

(G) Example of significantly enriched CHMP7 eCLIP-binding site on snRNA gene with size-matched input control reads on the same scale.

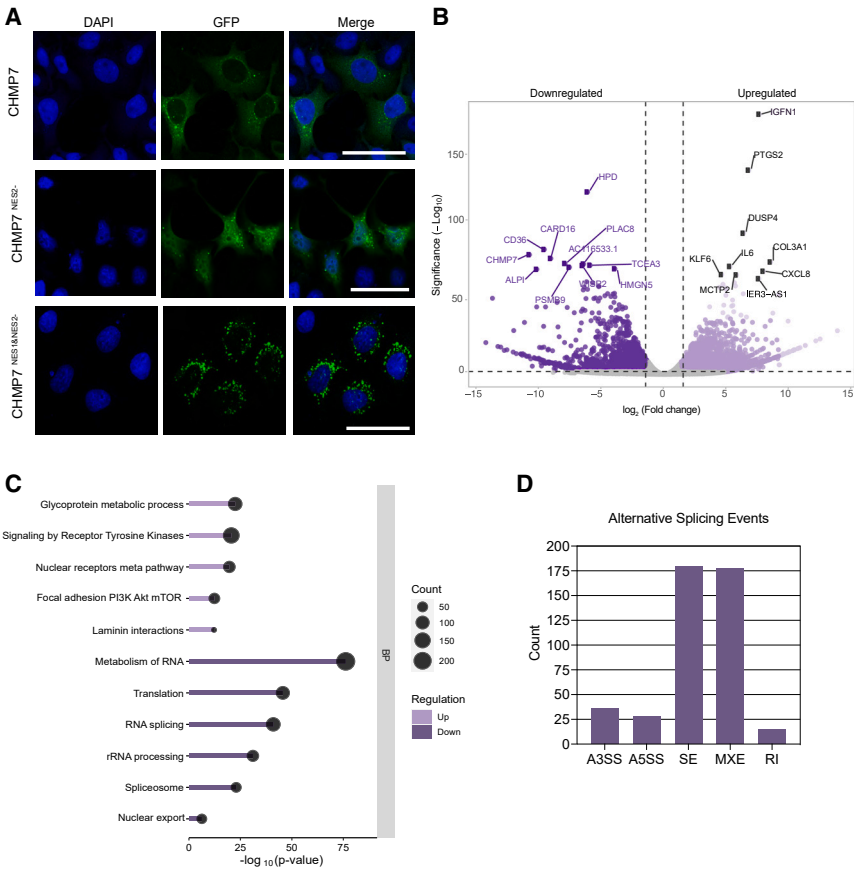

Figure 5. Downregulation of RNA processing upon CHMP7 nuclear accumulation in HeLa cells

(A) Immunofluorescence staining of GFP-CHMP7, helix 6 (GFP-CHMP7^{NES2-}), or helix 5 and helix 6 (GFP-CHMP7$^{NES1-\&NES2-}$) with nuclear DAPI signal in HeLa cells. Scale bars, 50 μm.

(B) Volcano plot comparing differentially expressed transcripts from RNA-seq analysis of GFP- GFP-CHMP7^{NES2-} vs. GFP-CHMP7 transient expression, with p value threshold of 0.05 and fold change of 2 as cutoffs.

(C) GO analysis of downregulated and upregulated transcripts from volcano plot in (B) (Table S3).

(D) Distribution of classes of differentially changing alternative splicing events (FDR $\leq 0.05 + |\Delta\Psi| < 0.1$) comparing GFP-CHMP7^{NES2-} with GFP-CHMP7 expression.

context of SmD1 KD. Our findings revealed a reduction in the total abundance of full-length STMN2 mRNA, accompanied by a corresponding increase in truncated STMN2 mRNA (Figures S5C and S5D). Furthermore, to understand whether SmD1 KD causes downstream consequences on MN health, we observed glutamate-induced excitotoxicity with SmD1 KD in control iPSCs (Figure S5E). Conversely, to investigate whether the restoration of SmD1 could influence STMN2 expression patterns, we demonstrate that overexpression of SmD1 led to the restoration of STMN2 levels while concurrently reducing truncated STMN2 mRNA abundance (Figures 7D and 7E). Furthermore, we noted a substantial restoration of CHMP7 cytoplasmic localization following the increase in SmD1 levels, (Figures 7F, 7G, and S5F).

Prior proteomics work in sALS patient tissue depicted that SMN protein is reduced, in correlation with increased disease severity.[53] This finding aligns with recent research conducted on sALS spinal cord tissues, where laser capture microdissection and proteomic analysis unveiled a striking decrease in the abundance of SMN component SmD1.[54] Further supporting these observations, we observed a significant reduction of SmD1 mRNA levels in ALS (12 sALS and 8 C9ORF72) day 32 iPSC-MNs relative to controls (Figure 7H). We have also noticed a reduction of NOVA2 and TAF15 expression, but not DHX8 and XPO7 in these analyses (Figure S6). Collectively, these data provide compelling evidence that the snRNP splicing factor SmD1 plays a pivotal role in modulating the nuclear localization of CHMP7.

Pharmacological inhibition of snRNP assembly leads to CHMP7 nuclear localization

As an alternative to the genetic depletion of SmD1 protein, we next determined whether pharmacological inhibition of snRNP assembly would alter nuclear/cytoplasmic translocation using live-cell imaging. Live-cell microscopy of GFP-CHMP7 and mCherry-TDP43 was conducted in HeLa cells subjected to either mock treatment or treatment with a commercially available SMN inhibitor as previously discovered (2 h at 200 μM).[55] Intriguingly, GFP-CHMP7 rapidly localized to the nucleus following snRNP inhibition (Figures 8A and 8B). Over a 2-h treatment period, CHMP7 coalesced at the nuclear periphery, a phenomenon previously observed during the maintenance of nuclear envelope homeostasis during cell division.[37,56,57] Endogenously, we performed the same experiment and observed a robust pattern of nuclear influx of CHMP7 (Figures 8C and S7A) and changes in NPC barrier function (Figure S7B). As for TDP-43, we observed subtle changes in the nuclear abundance of TDP-43 over the 2-h period, with no significant translocation evident (Figure 8A). However, after a 24-h treatment with the SMN inhibitor at 30 μM, we began to observe endogenous TDP-43 translocating to the cytoplasm with IF (Figures S7C and S7D). Our findings build upon previous research,[4] supporting the interpretation that cytoplasmic TDP-43 translocation follows the aberrant nuclear localization of CHMP7 and associated nuclear pore injury (Figure 8D).

DISCUSSION

Abnormal nuclear accumulation of CHMP7 can initiate NPC injury and cause defects in NCT, resulting in TDP-43 dysfunction and mislocalization in human ALS neurons.[4] Recent studies have demonstrated that SUN1 mediated alterations to NPC permeability barrier integrity facilitate increased nuclear influx of

Please cite this article in press as: Al-Azzam et al., Inhibition of RNA splicing triggers CHMP7 nuclear entry, impacting TDP-43 function and leading to the onset of ALS cellular phenotypes, Neuron (2024), https://doi.org/10.1016/j.neuron.2024.10.007

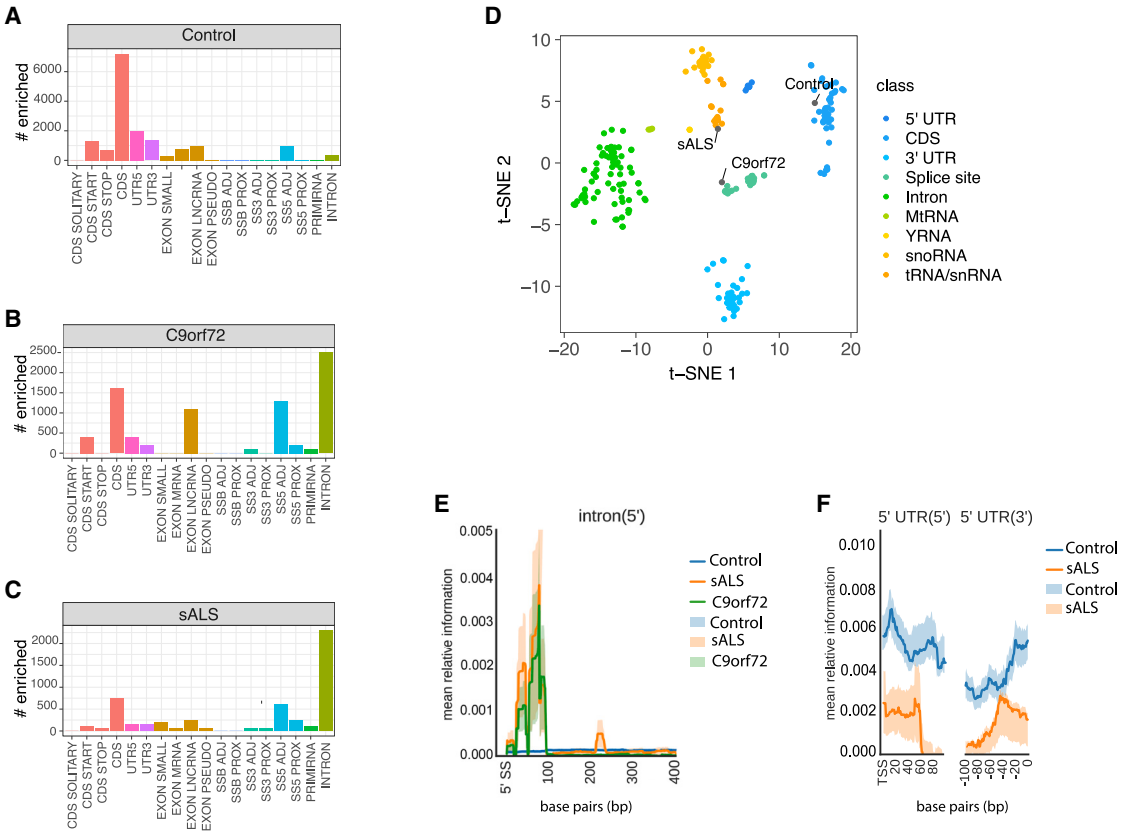

Figure 6. Alterations in CHMP7 protein-RNA landscape in ALS iPSC-MNs

(A–C) Number of enriched CHMP7 binding windows across control, C9orf72, and sALS lines.

(D) Skipper t-distributed stochastic neighbor embedding (t-SNE) analysis of CHMP7-enriched binding in genic features across control, C9orf72, and sALS, with ENCODE eCLIP data colored by target preferences in the background.

(E) Mean relative information around introns for CHMP7 control, C9orf72, and sALS in lines.

(F) Mean relative information around 5′ UTR for CHMP7 in control and sALS lines.

CHMP7 in sALS.[58] However, the mechanisms and molecular players underlying regulation of CHMP7 subcellular distribution remain unknown and are of critical importance to our understanding of early pathogenesis of ALS.

Here, we employed high-throughput imaging-based custom RBP-focused CRISPR-Cas9-based knockout screening technologies utilizing microRaft arrays to identify molecular regulators of CHMP7 nuclear localization. This screening approach identified 55 novel candidates influencing the subcellular distribution of CHMP7, many of which have been previously implicated in RNA processing, translation, and splicing regulation. Our subsequent investigations focused on the validation of 23 identified candidates, selected based on their potential relevance to ALS pathogenesis and roles in RNA processing. These validation experiments revealed that depletion of specific RNA processing proteins, including export factors, helicases, and splicing proteins, led to a substantial increase in CHMP7 nuclear localization. Notably, SNRPD1/SmD1 emerged as a primary and unexpected candidate in controlling CHMP7's subcellular localization, showcasing one pathway that can influence CHMP7 translocation specifically.

To explore the RNA-binding capabilities of CHMP7, we conducted a transcriptome-wide analysis of its RNA substrates. Our findings revealed CHMP7's affinity for both snRNAs (RNU1 and RNU2) and RNAs that encode for protein-coding genes, particularly in exonic regions and the 5′ UTR (Figures 4C, 4F, and 4G). Although we did not observe direct binding of CHMP7 to SmD1, we confirmed its interaction with snRNAs, specifically RNU1 and RNU2, which are components of the U1 spliceosome. Interestingly, when CHMP7 abnormally localizes to the nucleus in ALS iPSC-MNs, its binding profile shifts to intronic regions, suggesting an interaction with pre-RNA likely due to its nuclear localization. Our discovery further underscores the notion of pathway-level dysregulation in cellular RNA splicing processes as a link to the progression in the context of ALS as previously have been reported.[59,60]

We show that alterations in the assembly of snRNPs, influenced by SMN complex inhibition and the depletion of splicing factors like SmD1, modulate CHMP7's subcellular distribution. This phenomenon, also accompanied by nuclear pore injury, suggests a causal relationship between RNA processing disruptions, CHMP7 localization, and NPC integrity. Ultimately, these

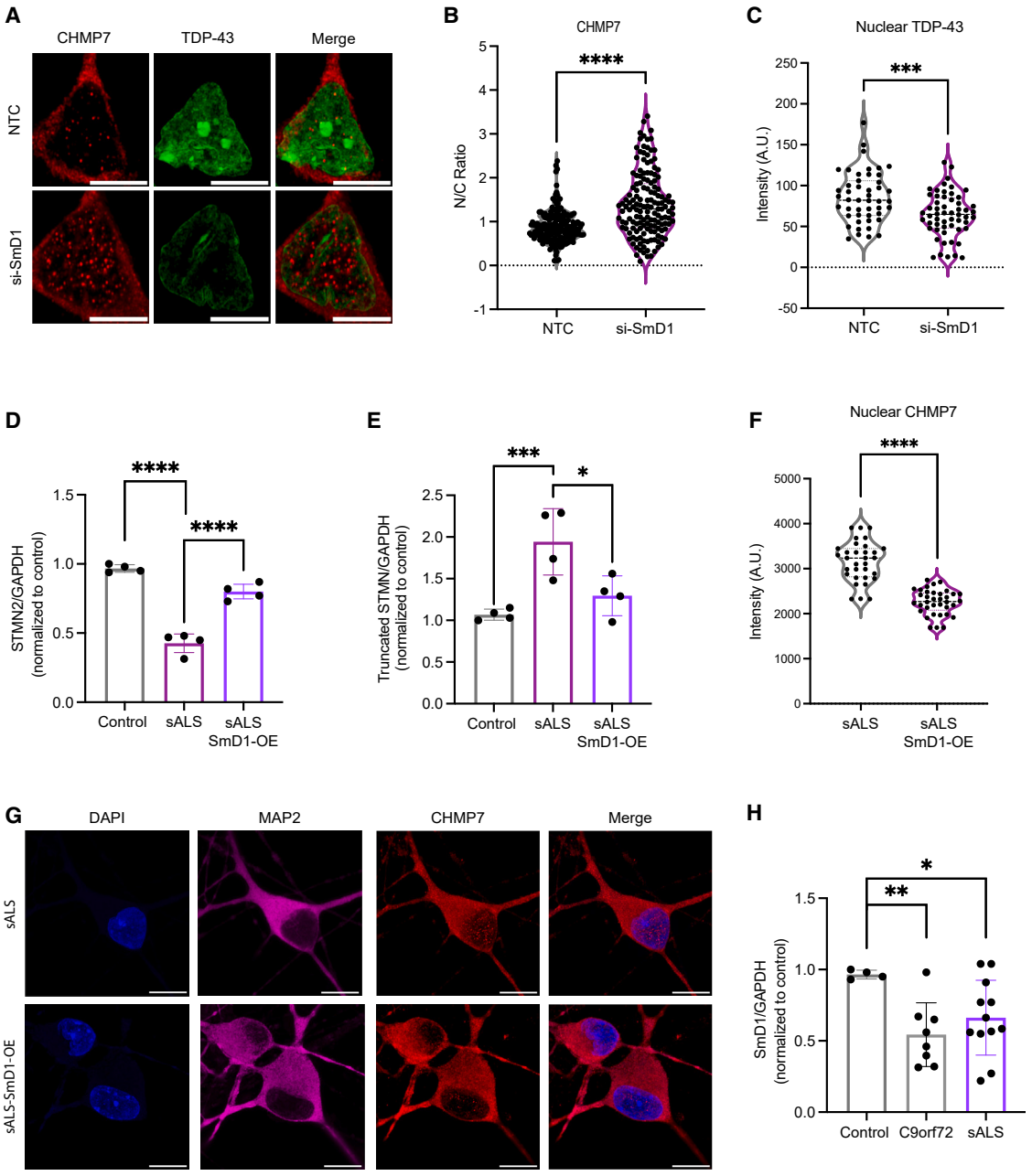

Figure 7. Overexpression of SmD1 can sufficiently rescue CHMP7 cytoplasmic levels in sALS iPSC-MNs

(A) Immunofluorescence of day 28 iPSC-MNs with either NTC and si-SmD1, stained with CHMP7 and TDP-43. Showing CHMP7 nuclear localization in SmD1 KD and reduction in nuclear TDP-43. Scale bars, 10 μm.

(B) Quantification of nuclear (N) to cytoplasmic (C) CHMP7 intensity in MNs (n = 3, ~150 cells total).

(C) Quantification of nuclear TDP-43 levels with si-SmD1 compared with NTC (n = 3, ~50 cells total).

(D and E) Overexpression of control plasmid and SmD1 open reading frame at day 36 in sALS lines showing mRNA levels for STMN2 and truncated STMN2 (n = 4). The data are presented as the mean ± SD. Significance was assessed using the Student's test (*p < 0.05, ***p < 0.001, ****p < 0.0001).

(F) Quantification of nuclear CHMP7 in neurons overexpressing SmD1 (n = 3, ~35 cells total).

(G) Immunofluorescence staining of neurons overexpressing SmD1 in sALS at day 36, stained with CHMP7, MAP2, and DAPI. Scale bars, 10 μm.

(H) mRNA levels of SmD1 in 12 sALS lines and 8 C9orf72, normalized to GAPDH and control lines at day 32. The data are presented as the mean ± SD. Significance was assessed using Student's t test (*p < 0.05, ***p < 0.001).

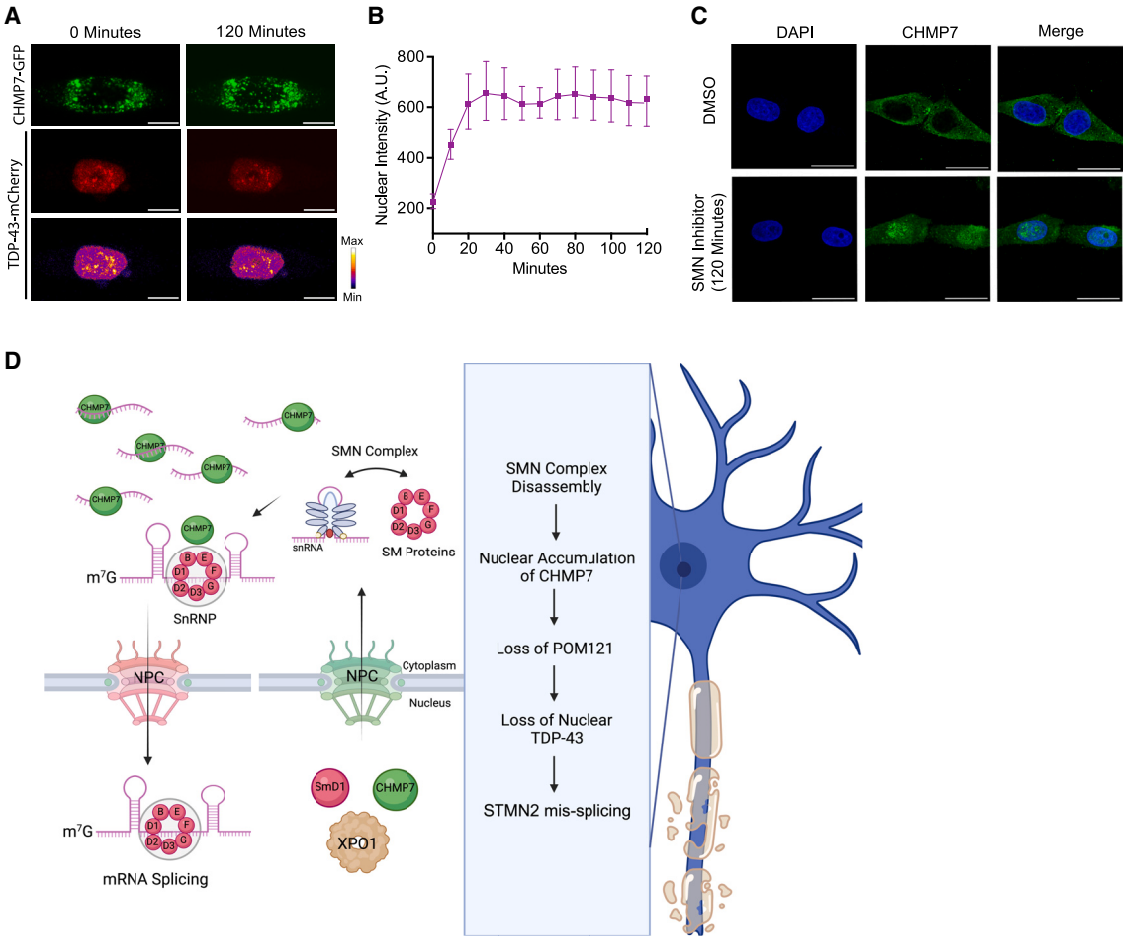

Figure 8. Perturbation of SMN-complex-dependent snRNP assembly modulates CHMP7 nuclear influx localization and alters NPC proteins

(A) Live-cell imaging of GFP-CHMP7 and TDP-43-mCherry at 0 and 120 min post-SMN inhibitor treatment. Heatmap of fluorescent intensity ratio of TDP-43 at 0 min and at 120 min. Scale bars, 20 μm.

(B) x axis indicates minutes (min); 0 min is prior to SMN inhibitor treatment. Nuclear GFP intensity, cells quantified, is ∼12 used and averaged from three independent experiments. Error bars show ± SD.

(C) Immunofluorescence analysis of CHMP7 (green) and DAPI with DMSO or SMN inhibitor in HeLa after 2 h (n = 3). Scale bars, 100 μm.

(D) Proposed mechanism of action. Created with BioRender.com.

events contribute to decreased motor survival, triggering a cascade in ALS neurodegeneration.

In our pursuit to understand the interplay between SmD1 and TDP-43 function, we demonstrated that overexpression of SmD1 restored total STMN2 expression levels and reduced truncated STMN2 mRNA. Significantly, this exogenous expression of SmD1 also led to a substantial restoration of CHMP7's cytoplasmic localization, implying that SMN dysfunction may contribute to abnormal nuclear localization of CHMP7 in disease. Our focus on SmD1, a splicing factor within the SMN snRNP, reveals insights into the modulation of CHMP7 subcellular distribution, shedding light on one mechanism underlying sALS.

Disruptions in RNA processing, including perturbations in snRNPs and defects in axonal transport, have been previously linked to ALS pathogenesis.[61,62] Alterations in SMN1 copy number, such as gene deletions or duplications, increase the risk of developing sALS.[63,64] These changes likely disrupt normal SMN protein levels, resulting in heightened vulnerability of MNs to degeneration. SMN deficiency has been shown to worsen the severity of the phenotype in mutant SOD1 mice.[65] Furthermore, a reduction in the number of Gemins due to decreased SMN levels is a common feature of both SMA and ALS.[66] Even though both are distinct MN diseases, SMA and ALS have significant molecular overlaps. First, components of the SMN complex, including SMN itself, have been identified as key players in the interactomes of various ALS-related proteins, such as SOD1, TDP-43, FUS, and dipeptide repeat proteins from C9orf72 gene expansions.[22,67] TDP-43 and FUS, which localize to Gemins—nuclear bodies rich in SMN complexes[68]—further emphasize these connections. Second, MNs derived from ALS patients show varied SMN levels, with those having lower levels being more susceptible to cell death.[69] Finally, past studies in Drosophila have underscored SmD1's role in RNAi and antiviral immunity,[70] emphasizing the importance of most SMN complex

proteins for neuronal survival, as their mutations or KDs can significantly reduce lifespan in Drosophila. Our study illuminates a key mechanistic connection between SMN and snRNP complex assembly and modulation of CHMP7 localization and subsequent NPC injury, integrating all these previous observations for the first time.

In summary, RNA metabolism defects are increasingly implicated in the pathogenesis of MN diseases. This work facilitates the understanding of the RNA complex components involvement in ALS and raise the need for further exploring their contribution as potential susceptibility genes or risk factors for ALS or SMA. Furthermore, while therapeutics elevating SMN levels show promise in treating SMA, their effectiveness in ALS patients requires further investigation.

Limitations of the study

In this study, we performed CRaft-ID in HeLa cells. Although the nuclear architecture is sufficiently similar enough to other cell types such as neurons, there are still cell-type-specific differences we can consider in the future. Additionally, we concentrated on understanding the role of the SMN complex in CHMP7 nuclear entry as one pathway to explain this phenomenon. However, it is possible that multiple pathways are involved in coordinating CHMP7 nuclear influx. Finally, CHMP7 nuclear localization in sALS was not observed in all diseased iPSC lines. Therefore, only the lines that exhibited localization were identified, screened, and selected for further biochemical assays.

RESOURCE AVAILABILITY

Lead contact

Further information and requests for resources and reagents should be directed to and will be fulfilled by the lead contact, Gene W. Yeo (geneyeo@ucsd.edu).

Materials availability

This study did not generate new unique reagents.

Data and code availability

- RNA-seq, eCLIP, have been deposited at GEO and are publicly available as of the date of publication. Mass spectrometry raw data have been deposited at MassIVE. Accession numbers are listed in the key resources table.
- This paper does not report original code.
- Any additional information required to reanalyze the data reported in this paper is available from the lead contact upon request.

ACKNOWLEDGMENTS

We thank members of the Yeo lab for helpful suggestions on the work and the manuscript. G.W.Y. is supported by NIH (R01 HG004659 and U24 HG009889) and an Allen Distinguished Investigator Award, a Paul G. Allen Frontiers Group advised grant of the Paul G. Allen Foundation. M.J. is funded by the NIH (R35 GM128802, R01 AG071869, and R01 HG012216) and the NSF (MCB-2224211). O.M. was supported by a Gruss-Lipper postdoctoral fellowship. This work was supported by a Chan Zuckerberg Initiative Collaborative Science Award to G.W.Y. and J.D.R. This work was partially supported by the Waitt Advanced Biophotonics Core Facility of the Salk Institute with funding from NIH-NCI CCSG (P30 CA01495), NIH-NIA San Diego Nathan Shock Center (P30 AG068635), and the Waitt Foundation. U.M. is also supported by the CZI Imaging Scientist Award from the Chan Zuckerberg Initiative DAF, an advised fund of Silicon Valley Community Foundation. We thank Dr. Jeremy G. Carlton for sending the initial CHMP7 mutants. We acknowledge Cell Microsystems for the use of the CellRaft AIR System. We thank Dr. Beate Winner and Dr. Holger Wend for providing the sporadic ALS lines.

AUTHOR CONTRIBUTIONS

G.W.Y. conceived the study. N.A.-A. optimized the screen, collected data, analyzed data, and visualized results. N.A.-A., J.H.T., and V.G. designed wet-lab validation experiments. N.A.-A., J.H.T., V.G., L.A.S., C.B.N., J.T.N., D.C.L., A.A.M., B.L., W.J., A.A., O.M., J.R.M., W.F., C.R.S., E.R., A.Q.V., S.M.B., and Y.L.M. carried out the experimental and computational work. N.A.-A. wrote the original manuscript draft. G.W.Y. reviewed and edited the manuscript. A.N.C. and J.D.R. provided reagents and acquired funding. U.M., C.R.S., and E.R. designed and performed the imaging and analysis experiments with N.A.-A. G.W.Y. acquired the funding and supervised the study.

DECLARATION OF INTERESTS

G.W.Y. is a co-founder, a member of the board of directors, on the scientific advisory board, an equity holder, and a paid consultant for Eclipse BioInnovations. G.W.Y.'s interests have been reviewed and approved by the University of California San Diego in accordance with its conflict-of-interest policies.

STAR★METHODS

Detailed methods are provided in the online version of this paper and include the following:

- KEY RESOURCES TABLE
- EXPERIMENTAL MODEL AND STUDY PARTICIPANT DETAILS
  - Induced pluripotent stem cells, differentiated motoneurons, and cell lines
- METHOD DETAILS
  - Generating GFP-CHMP7 fluorescently labeled HeLa cells
  - Viral infection of HeLa cells with CRISPR-Cas9 library
  - Preparation of CRISPR library virus
  - Determination of multiplicity of infection (MOI)
  - MicroRaft cell culture
  - Guide identification of target wells
  - siRNA transfections validation of candidates
  - Immunofluorescence
  - Imaging
  - Time-lapse imaging with SMN inhibitor
  - Dextran exclusion
  - Nuclear pore complex imaging
  - Glutamate toxicity
  - Western blot
  - Immunoprecipitations
  - LC-MS/MS DIA
- QUANTIFICATION AND STATISTICAL ANALYSIS

SUPPLEMENTAL INFORMATION

Supplemental information can be found online at https://doi.org/10.1016/j.neuron.2024.10.007.

Received: February 11, 2024
Revised: July 8, 2024
Accepted: October 4, 2024
Published: October 31, 2024

REFERENCES

1. Wijesekera, L.C., and Leigh, P.N. (2009). Amyotrophic lateral sclerosis. Orphanet J. Rare Dis. *4*, 3. https://doi.org/10.1186/1750-1172-4-3.
2. Taylor, J.P., Brown, R.H., Jr., and Cleveland, D.W. (2016). Decoding ALS: from genes to mechanism. Nature *539*, 197–206. https://doi.org/10.1038/nature20413.
3. Zhang, K., Donnelly, C.J., Haeusler, A.R., Grima, J.C., Machamer, J.B., Steinwald, P., Daley, E.L., Miller, S.J., Cunningham, K.M., Vidensky, S., et al. (2015). The C9orf72 repeat expansion disrupts nucleocytoplasmic transport. Nature *525*, 56–61. https://doi.org/10.1038/nature14973.
4. Coyne, A.N., Baskerville, V., Zaepfel, B.L., Dickson, D.W., Rigo, F., Bennett, F., Lusk, C.P., and Rothstein, J.D. (2021). Nuclear accumulation of CHMP7 initiates nuclear pore complex injury and subsequent TDP-43 dysfunction in sporadic and familial ALS. Sci. Transl. Med. *13*, eabe1923. https://doi.org/10.1126/scitranslmed.abe1923.
5. Hayes, L.R., Duan, L., Bowen, K., Kalab, P., and Rothstein, J.D. (2020). C9orf72 arginine-rich dipeptide repeat proteins disrupt karyopherin-mediated nuclear import. eLife *9*, e51685. https://doi.org/10.7554/eLife.51685.
6. D'Angelo, M.A., Raices, M., Panowski, S.H., and Hetzer, M.W. (2009). Age-dependent deterioration of nuclear pore complexes causes a loss of nuclear integrity in postmitotic cells. Cell *136*, 284–295. https://doi.org/10.1016/j.cell.2008.11.037.
7. Yi, H., Mu, L., Shen, C., Kong, X., Wang, Y., Hou, Y., and Zhang, R. (2020). Negative cooperativity between Gemin2 and RNA provides insights into RNA selection and the SMN complex's release in snRNP assembly. Nucleic Acids Res. *48*, 895–911. https://doi.org/10.1093/nar/gkz1135.
8. Tang, X., Bharath, S.R., Piao, S., Tan, V.Q., Bowler, M.W., and Song, H. (2016). Structural basis for specific recognition of pre-snRNA by Gemin5. Cell Res. *26*, 1353–1356. https://doi.org/10.1038/cr.2016.133.
9. Xu, C., Ishikawa, H., Izumikawa, K., Li, L., He, H., Nobe, Y., Yamauchi, Y., Shahjee, H.M., Wu, X.H., Yu, Y.T., et al. (2016). Structural insights into Gemin5-guided selection of pre-snRNAs for snRNP assembly. Genes Dev. *30*, 2376–2390. https://doi.org/10.1101/gad.288340.116.
10. Pillai, R.S., Grimmler, M., Meister, G., Will, C.L., Lührmann, R., Fischer, U., and Schümperli, D. (2003). Unique Sm core structure of U7 snRNPs: assembly by a specialized SMN complex and the role of a new component, Lsm11, in histone RNA processing. Genes Dev. *17*, 2321–2333. https://doi.org/10.1101/gad.274403.
11. Meister, G., Hannus, S., Plöttner, O., Baars, T., Hartmann, E., Fakan, S., Laggerbauer, B., and Fischer, U. (2001). SMNrp is an essential pre-mRNA splicing factor required for the formation of the mature spliceosome. EMBO J. *20*, 2304–2314. https://doi.org/10.1093/emboj/20.9.2304.
12. Will, C.L., and Lührmann, R. (2001). Spliceosomal UsnRNP biogenesis, structure and function. Curr. Opin. Cell Biol. *13*, 290–301. https://doi.org/10.1016/s0955-0674(00)00211-8.
13. Patel, A.A., and Steitz, J.A. (2003). Splicing double: insights from the second spliceosome. Nat. Rev. Mol. Cell Biol. *4*, 960–970. https://doi.org/10.1038/nrm1259.
14. Mandelboim, M., Barth, S., Biton, M., Liang, X.H., and Michaeli, S. (2003). Silencing of Sm proteins in Trypanosoma brucei by RNA interference captured a novel cytoplasmic intermediate in spliced leader RNA biogenesis. J. Biol. Chem. *278*, 51469–51478. https://doi.org/10.1074/jbc.M308997200.
15. Grimm, C., Chari, A., Pelz, J.P., Kuper, J., Kisker, C., Diederichs, K., Stark, H., Schindelin, H., and Fischer, U. (2013). Structural basis of assembly chaperone-mediated snRNP formation. Mol. Cell *49*, 692–703. https://doi.org/10.1016/j.molcel.2012.12.009.
16. Massenet, S., Pellizzoni, L., Paushkin, S., Mattaj, I.W., and Dreyfuss, G. (2002). The SMN complex is associated with snRNPs throughout their cytoplasmic assembly pathway. Mol. Cell. Biol. *22*, 6533–6541. https://doi.org/10.1128/MCB.22.18.6533-6541.2002.
17. Liu, Q., Fischer, U., Wang, F., and Dreyfuss, G. (1997). The spinal muscular atrophy disease gene product, SMN, and its associated protein SIP1 are in a complex with spliceosomal snRNP proteins. Cell *90*, 1013–1021. https://doi.org/10.1016/s0092-8674(00)80367-0.
18. Harada, Y., Sutomo, R., Sadewa, A.H., Akutsu, T., Takeshima, Y., Wada, H., Matsuo, M., and Nishio, H. (2002). Correlation between SMN2 copy number and clinical phenotype of spinal muscular atrophy: three SMN2 copies fail to rescue some patients from the disease severity. J. Neurol. *249*, 1211–1219. https://doi.org/10.1007/s00415-002-0811-4.
19. Shukla, S., and Parker, R. (2016). Hypo- and Hyper-Assembly Diseases of RNA-Protein Complexes. Trends Mol. Med. *22*, 615–628. https://doi.org/10.1016/j.molmed.2016.05.005.
20. Shan, X., Chiang, P.M., Price, D.L., and Wong, P.C. (2010). Altered distributions of Gemini of coiled bodies and mitochondria in motor neurons of TDP-43 transgenic mice. Proc. Natl. Acad. Sci. USA *107*, 16325–16330. https://doi.org/10.1073/pnas.1003459107.
21. Gertz, B., Wong, M., and Martin, L.J. (2012). Nuclear localization of human SOD1 and mutant SOD1-specific disruption of survival motor neuron protein complex in transgenic amyotrophic lateral sclerosis mice. J. Neuropathol. Exp. Neurol. *71*, 162–177. https://doi.org/10.1097/NEN.0b013e318244b635.
22. Tsuiji, H., Iguchi, Y., Furuya, A., Kataoka, A., Hatsuta, H., Atsuta, N., Tanaka, F., Hashizume, Y., Akatsu, H., Murayama, S., et al. (2013). Spliceosome integrity is defective in the motor neuron diseases ALS and SMA. EMBO Mol. Med. *5*, 221–234. https://doi.org/10.1002/emmm.201202303.
23. Wheeler, E.C., Vu, A.Q., Einstein, J.M., DiSalvo, M., Ahmed, N., Van Nostrand, E.L., Shishkin, A.A., Jin, W., Allbritton, N.L., and Yeo, G.W. (2020). Pooled CRISPR screens with imaging on microRaft arrays reveals stress granule-regulatory factors. Nat. Methods *17*, 636–642. https://doi.org/10.1038/s41592-020-0826-8.
24. Fornerod, M., and Ohno, M. (2002). Exportin-mediated nuclear export of proteins and ribonucleoproteins. Results Probl. Cell Differ. *35*, 67–91. https://doi.org/10.1007/978-3-540-44603-3_4.
25. Vietri, M., Schultz, S.W., Bellanger, A., Jones, C.M., Petersen, L.I., Raiborg, C., Skarpen, E., Pedurupillay, C.R.J., Kjos, I., Kip, E., et al. (2020). Unrestrained ESCRT-III drives micronuclear catastrophe and chromosome fragmentation. Nat. Cell Biol. *22*, 856–867. https://doi.org/10.1038/s41556-020-0537-5.
26. Krus, K.L., Strickland, A., Yamada, Y., Devault, L., Schmidt, R.E., Bloom, A.J., Milbrandt, J., and DiAntonio, A. (2022). Loss of Stathmin-2, a hallmark of TDP-43-associated ALS, causes motor neuropathy. Cell Rep. *39*, 111001. https://doi.org/10.1016/j.celrep.2022.111001.
27. Melamed, Z., López-Erauskin, J., Baughn, M.W., Zhang, O., Drenner, K., Sun, Y., Freyermuth, F., McMahon, M.A., Beccari, M.S., Artates, J.W., et al. (2019). Premature polyadenylation-mediated loss of stathmin-2 is a hallmark of TDP-43-dependent neurodegeneration. Nat. Neurosci. *22*, 180–190. https://doi.org/10.1038/s41593-018-0293-z.
28. Klim, J.R., Williams, L.A., Limone, F., Guerra San Juan, I., Davis-Dusenbery, B.N., Mordes, D.A., Burberry, A., Steinbaugh, M.J., Gamage, K.K., Kirchner, R., et al. (2019). ALS-implicated protein TDP-43 sustains levels of STMN2, a mediator of motor neuron growth and repair. Nat. Neurosci. *22*, 167–179. https://doi.org/10.1038/s41593-018-0300-4.
29. Li, W., Xu, H., Xiao, T., Cong, L., Love, M.I., Zhang, F., Irizarry, R.A., Liu, J.S., Brown, M., and Liu, X.S. (2014). MAGeCK enables robust identification of essential genes from genome-scale CRISPR/Cas9 knockout screens. Genome Biol. *15*, 554. https://doi.org/10.1186/s13059-014-0554-4.
30. Aksu, M., Pleiner, T., Karaca, S., Kappert, C., Dehne, H.J., Seibel, K., Urlaub, H., Bohnsack, M.T., and Görlich, D. (2018). Xpo7 is a broad-spectrum exportin and a nuclear import receptor. J. Cell Biol. *217*, 2329–2340. https://doi.org/10.1083/jcb.201712013.
31. Xu, F., Jia, M., Li, X., Tang, Y., Jiang, K., Bao, J., and Gu, Y. (2021). Exportin-4 coordinates nuclear shuttling of TOPLESS family transcription

corepressors to regulate plant immunity. Plant Cell *33*, 697–713. https://doi.org/10.1093/plcell/koaa047.

32. Felisberto-Rodrigues, C., Thomas, J.C., McAndrew, C., Le Bihan, Y.V., Burke, R., Workman, P., and van Montfort, R.L.M. (2019). Structural and functional characterisation of human RNA helicase DHX8 provides insights into the mechanism of RNA-stimulated ADP release. Biochem. J. *476*, 2521–2543. https://doi.org/10.1042/BCJ20190383.
33. Weber, G., Trowitzsch, S., Kastner, B., Lührmann, R., and Wahl, M.C. (2010). Functional organization of the Sm core in the crystal structure of human U1 snRNP. EMBO J. *29*, 4172–4184. https://doi.org/10.1038/emboj.2010.295.
34. Chu, Q., Wang, J., Du, Y., Zhou, T., Shi, A., Xiong, J., Ji, W.K., and Deng, L. (2023). Oligomeric CHMP7 mediates three-way ER junctions and ER-mitochondria interactions. Cell Death Differ. *30*, 94–110. https://doi.org/10.1038/s41418-022-01048-2.
35. Webster, B.M., Colombi, P., Jäger, J., and Lusk, C.P. (2014). Surveillance of nuclear pore complex assembly by ESCRT-III/Vps4. Cell *159*, 388–401. https://doi.org/10.1016/j.cell.2014.09.012.
36. Webster, B.M., Thaller, D.J., Jäger, J., Ochmann, S.E., Borah, S., and Lusk, C.P. (2016). Chm7 and Heh1 collaborate to link nuclear pore complex quality control with nuclear envelope sealing. EMBO J. *35*, 2447–2467. https://doi.org/10.15252/embj.201694574.
37. Gu, M., LaJoie, D., Chen, O.S., von Appen, A., Ladinsky, M.S., Redd, M.J., Nikolova, L., Bjorkman, P.J., Sundquist, W.I., Ullman, K.S., and Frost, A. (2017). LEM2 recruits CHMP7 for ESCRT-mediated nuclear envelope closure in fission yeast and human cells. Proc. Natl. Acad. Sci. USA *114*, E2166–E2175. https://doi.org/10.1073/pnas.1613916114.
38. Olmos, Y., Perdrix-Rosell, A., and Carlton, J.G. (2016). Membrane Binding by CHMP7 Coordinates ESCRT-III-Dependent Nuclear Envelope Reformation. Curr. Biol. *26*, 2635–2641. https://doi.org/10.1016/j.cub.2016.07.039.
39. Liu, Q., and Dreyfuss, G. (1996). A novel nuclear structure containing the survival of motor neurons protein. EMBO J. *15*, 3555–3565. https://doi.org/10.1002/j.1460-2075.1996.tb00725.x.
40. Jin, W., Brannan, K.W., Kapeli, K., Park, S.S., Tan, H.Q., Gosztyla, M.L., Mujumdar, M., Ahdout, J., Henroid, B., Rothamel, K., et al. (2023). HydRA: Deep-learning models for predicting RNA-binding capacity from protein interaction association context and protein sequence. Mol. Cell *83*, 2595–2611.e11. https://doi.org/10.1016/j.molcel.2023.06.019.
41. Van Nostrand, E.L., Pratt, G.A., Shishkin, A.A., Gelboin-Burkhart, C., Fang, M.Y., Sundararaman, B., Blue, S.M., Nguyen, T.B., Surka, C., Elkins, K., et al. (2016). Robust transcriptome-wide discovery of RNA-binding protein binding sites with enhanced CLIP (eCLIP). Nat. Methods *13*, 508–514. https://doi.org/10.1038/nmeth.3810.
42. Boyle, E.A., Her, H.L., Mueller, J.R., Naritomi, J.T., Nguyen, G.G., and Yeo, G.W. (2023). Skipper analysis of eCLIP datasets enables sensitive detection of constrained translation factor binding sites. Cell Genomics *3*, 100317. https://doi.org/10.1016/j.xgen.2023.100317.
43. Van Nostrand, E.L., Freese, P., Pratt, G.A., Wang, X., Wei, X., Xiao, R., Blue, S.M., Chen, J.Y., Cody, N.A.L., Dominguez, D., et al. (2020). A large-scale binding and functional map of human RNA-binding proteins. Nature *583*, 711–719. https://doi.org/10.1038/s41586-020-2077-3.
44. Makarov, E.M., Owen, N., Bottrill, A., and Makarova, O.V. (2012). Functional mammalian spliceosomal complex E contains SMN complex proteins in addition to U1 and U2 snRNPs. Nucleic Acids Res. *40*, 2639–2652. https://doi.org/10.1093/nar/gkr1056.
45. Gatta, A.T., Olmos, Y., Stoten, C.L., Chen, Q., Rosenthal, P.B., and Carlton, J.G. (2021). CDK1 controls CHMP7-dependent nuclear envelope reformation. eLife *10*, e59999. https://doi.org/10.7554/eLife.59999.
46. Thaller, D.J., Allegretti, M., Borah, S., Ronchi, P., Beck, M., and Lusk, C.P. (2019). An ESCRT-LEM protein surveillance system is poised to directly monitor the nuclear envelope and nuclear transport system. eLife *8*, e45284. https://doi.org/10.7554/eLife.45284.
47. Her, H.L., Boyle, E., and Yeo, G.W. (2022). Metadensity: a background-aware python pipeline for summarizing CLIP signals on various transcriptomic sites. Bioinform. Adv. *2*, vbac083. https://doi.org/10.1093/bioadv/vbac083.
48. Krach, F., Wheeler, E.C., Regensburger, M., Boerstler, T., Wend, H., Vu, A.Q., Wang, R., Reischl, S., Boldt, K., Batra, R., et al. (2022). Aberrant NOVA1 function disrupts alternative splicing in early stages of amyotrophic lateral sclerosis. Acta Neuropathol. *144*, 413–435. https://doi.org/10.1007/s00401-022-02450-3.
49. Coyne, A.N., Zaepfel, B.L., Hayes, L., Fitchman, B., Salzberg, Y., Luo, E.C., Bowen, K., Trost, H., Aigner, S., Rigo, F., et al. (2020). G4C2 Repeat RNA Initiates a POM121-Mediated Reduction in Specific Nucleoporins in C9orf72 ALS/FTD. Neuron *107*, 1124–1140.e11. https://doi.org/10.1016/j.neuron.2020.06.027.
50. Chou, C.C., Zhang, Y., Umoh, M.E., Vaughan, S.W., Lorenzini, I., Liu, F., Sayegh, M., Donlin-Asp, P.G., Chen, Y.H., Duong, D.M., et al. (2018). TDP-43 pathology disrupts nuclear pore complexes and nucleocytoplasmic transport in ALS/FTD. Nat. Neurosci. *21*, 228–239. https://doi.org/10.1038/s41593-017-0047-3.
51. Rothstein, J.D., Warlick, C., and Coyne, A.N. (2023). Highly variable molecular signatures of TDP-43 loss of function are associated with nuclear pore complex injury in a population study of sporadic ALS patient iPSNs. Preprint at bioRxiv. https://doi.org/10.1101/2023.12.12.571299.
52. Jo, M., Lee, S., Jeon, Y.M., Kim, S., Kwon, Y., and Kim, H.J. (2020). The role of TDP-43 propagation in neurodegenerative diseases: integrating insights from clinical and experimental studies. Exp. Mol. Med. *52*, 1652–1662. https://doi.org/10.1038/s12276-020-00513-7.
53. Piao, Y., Hashimoto, T., Takahama, S., Kakita, A., Komori, T., Morita, T., Takahashi, H., Mizutani, T., and Oyanagi, K. (2011). Survival motor neuron (SMN) protein in the spinal anterior horn cells of patients with sporadic amyotrophic lateral sclerosis. Brain Res. *1372*, 152–159. https://doi.org/10.1016/j.brainres.2010.11.070.
54. Guise, A.J., Misal, S.A., Carson, R., Boekweg, H., Van Der Watt, D.V.D., Truong, T., Liang, Y., Chu, J.H., Welsh, N.C., Gagnon, J., et al. (2023). TDP-43-stratified single-cell proteomic profiling of postmortem human spinal motor neurons reveals protein dynamics in amyotrophic lateral sclerosis. Preprint at bioRxiv. https://doi.org/10.1101/2023.06.08.544233.
55. Liu, Y., Iqbal, A., Li, W., Ni, Z., Wang, Y., Ramprasad, J., Abraham, K.J., Zhang, M., Zhao, D.Y., Qin, S., et al. (2022). A small molecule antagonist of SMN disrupts the interaction between SMN and RNAP II. Nat. Commun. *13*, 5453. https://doi.org/10.1038/s41467-022-33229-5.
56. Stoten, C.L., and Carlton, J.G. (2018). ESCRT-dependent control of membrane remodelling during cell division. Semin. Cell Dev. Biol. *74*, 50–65. https://doi.org/10.1016/j.semcdb.2017.08.035.
57. Von Appen, A., LaJoie, D., Johnson, I.E., Trnka, M.J., Pick, S.M., Burlingame, A.L., Ullman, K.S., and Frost, A. (2020). LEM2 phase separation promotes ESCRT-mediated nuclear envelope reformation. Nature *582*, 115–118. https://doi.org/10.1038/s41586-020-2232-x.
58. Baskerville, V., Rapuri, S., Mehlhop, E., and Coyne, A.N. (2024). SUN1 facilitates CHMP7 nuclear influx and injury cascades in sporadic amyotrophic lateral sclerosis. Brain *147*, 109–121. https://doi.org/10.1093/brain/awad291.
59. Lehmkuhl, E.M., and Zarnescu, D.C. (2018). Lost in Translation: Evidence for Protein Synthesis Deficits in ALS/FTD and Related Neurodegenerative Diseases. Adv. Neurobiol. *20*, 283–301. https://doi.org/10.1007/978-3-319-89689-2_11.
60. Xue, Y.C., Ng, C.S., Xiang, P., Liu, H., Zhang, K., Mohamud, Y., and Luo, H. (2020). Dysregulation of RNA-Binding Proteins in Amyotrophic Lateral Sclerosis. Front. Mol. Neurosci. *13*, 78. https://doi.org/10.3389/fnmol.2020.00078.
61. Groen, E.J.N., Fumoto, K., Blokhuis, A.M., Engelen-Lee, J., Zhou, Y., van den Heuvel, D.M.A., Koppers, M., van Diggelen, F., van Heest, J., Demmers, J.A.A., et al. (2013). ALS-associated mutations in FUS disrupt

the axonal distribution and function of SMN. Hum. Mol. Genet. *22*, 3690–3704. https://doi.org/10.1093/hmg/ddt222.

62. Yasuda, K., and Mili, S. (2016). Dysregulated axonal RNA translation in amyotrophic lateral sclerosis. Wiley Interdiscip. Rev. RNA *7*, 589–603. https://doi.org/10.1002/wrna.1352.
63. Blauw, H.M., Barnes, C.P., van Vught, P.W., van Rheenen, W., Verheul, M., Cuppen, E., Veldink, J.H., and van den Berg, L.H. (2012). SMN1 gene duplications are associated with sporadic ALS. Neurology *78*, 776–780. https://doi.org/10.1212/WNL.0b013e318249f697.
64. Veldink, J.H., Kalmijn, S., Van der Hout, A.H., Lemmink, H.H., Groeneveld, G.J., Lummen, C., Scheffer, H., Wokke, J.H.J., and Van den Berg, L.H. (2005). SMN genotypes producing less SMN protein increase susceptibility to and severity of sporadic ALS. Neurology *65*, 820–825. https://doi.org/10.1212/01.wnl.0000174472.03292.dd.
65. Turner, B.J., Parkinson, N.J., Davies, K.E., and Talbot, K. (2009). Survival motor neuron deficiency enhances progression in an amyotrophic lateral sclerosis mouse model. Neurobiol. Dis. *34*, 511–517. https://doi.org/10.1016/j.nbd.2009.03.005.
66. Cauchi, R.J. (2014). Gem depletion: amyotrophic lateral sclerosis and spinal muscular atrophy crossover. CNS Neurosci. Ther. *20*, 574–581. https://doi.org/10.1111/cns.12242.
67. Yin, S., Lopez-Gonzalez, R., Kunz, R.C., Gangopadhyay, J., Borufka, C., Gygi, S.P., Gao, F.B., and Reed, R. (2017). Evidence that C9ORF72 Dipeptide Repeat Proteins Associate with U2 snRNP to Cause Mis-splicing in ALS/FTD Patients. Cell Rep. *19*, 2244–2256. https://doi.org/10.1016/j.celrep.2017.05.056.
68. Wang, I.F., Reddy, N.M., and Shen, C.K.J. (2002). Higher order arrangement of the eukaryotic nuclear bodies. Proc. Natl. Acad. Sci. USA *99*, 13583–13588. https://doi.org/10.1073/pnas.212483099.
69. Rodriguez-Muela, N., Litterman, N.K., Norabuena, E.M., Mull, J.L., Galazo, M.J., Sun, C., Ng, S.Y., Makhortova, N.R., White, A., Lynes, M.M., et al. (2017). Single-Cell Analysis of SMN Reveals Its Broader Role in Neuromuscular Disease. Cell Rep. *18*, 1484–1498. https://doi.org/10.1016/j.celrep.2017.01.035.
70. Xiong, X.P., Kurthkoti, K., Chang, K.Y., Lichinchi, G., De, N., Schneemann, A., MacRae, I.J., Rana, T.M., Perrimon, N., and Zhou, R. (2013). Core small nuclear ribonucleoprotein particle splicing factor SmD1 modulates RNA interference in Drosophila. Proc. Natl. Acad. Sci. USA *110*, 16520–16525. https://doi.org/10.1073/pnas.1315803110.
71. Gore, A., Li, Z., Fung, H.L., Young, J.E., Agarwal, S., Antosiewicz-Bourget, J., Canto, I., Giorgetti, A., Israel, M.A., Kiskinis, E., et al. (2011). Somatic coding mutations in human induced pluripotent stem cells. Nature *471*, 63–67. https://doi.org/10.1038/nature09805.
72. Dobin, A., Davis, C.A., Schlesinger, F., Drenkow, J., Zaleski, C., Jha, S., Batut, P., Chaisson, M., and Gingeras, T.R. (2013). STAR: ultrafast universal RNA-seq aligner. Bioinformatics Oxf. Engl. *29*, 15–21. https://doi.org/10.1093/bioinformatics/bts635.
73. Liao, Y., Smyth, G.K., and Shi, W. (2014). featureCounts: an efficient general purpose program for assigning sequence reads to genomic features. Bioinformatics Oxf. Engl. *30*, 923–930. https://doi.org/10.1093/bioinformatics/btt656.
74. Eden, E., Navon, R., Steinfeld, I., Lipson, D., and Yakhini, Z. (2009). GOrilla: a tool for discovery and visualization of enriched GO terms in ranked gene lists. BMC Bioinformatics *10*, 48. https://doi.org/10.1186/1471-2105-10-48.
75. Shen, S., Park, J.W., Lu, Z.X., Lin, L., Henry, M.D., Wu, Y.N., Zhou, Q., and Xing, Y. (2014). rMATS: robust and flexible detection of differential alternative splicing from replicate RNA-Seq data. Proc. Natl. Acad. Sci. USA *111*, E5593–E5601. https://doi.org/10.1073/pnas.1419161111.
76. Zhou, Y., Zhou, B., Pache, L., Chang, M., Khodabakhshi, A.H., Tanaseichuk, O., Benner, C., and Chanda, S.K. (2019). Metascape provides a biologist-oriented resource for the analysis of systems-level datasets. Nat. Commun. *10*, 1523. https://doi.org/10.1038/s41467-019-09234-6.
77. Heinz, S., Benner, C., Spann, N., Bertolino, E., Lin, Y.C., Laslo, P., Cheng, J.X., Murre, C., Singh, H., and Glass, C.K. (2010). Simple combinations of lineage-determining transcription factors prime cis-regulatory elements required for macrophage and B cell identities. Mol. Cell *38*, 576–589. https://doi.org/10.1016/j.molcel.2010.05.004.
78. Bruderer, R., Bernhardt, O.M., Gandhi, T., Miladinović, S.M., Cheng, L.Y., Messner, S., Ehrenberger, T., Zanotelli, V., Butscheid, Y., Escher, C., et al. (2015). Extending the limits of quantitative proteome profiling with data-independent acquisition and application to acetaminophen-treated three-dimensional liver microtissues. Mol. Cell. Proteomics *14*, 1400–1410. https://doi.org/10.1074/mcp.M114.044305.
79. Robinson, J.T., Thorvaldsdóttir, H., Winckler, W., Guttman, M., Lander, E.S., Getz, G., and Mesirov, J.P. (2011). Integrative genomics viewer. Nat. Biotechnol. *29*, 24–26. https://doi.org/10.1038/nbt.1754.
80. Schindelin, J., Arganda-Carreras, I., Frise, E., Kaynig, V., Longair, M., Pietzsch, T., Preibisch, S., Rueden, C., Saalfeld, S., Schmid, B., et al. (2012). Fiji: an open-source platform for biological-image analysis. Nat. Methods *9*, 676–682. https://doi.org/10.1038/nmeth.2019.
81. Markmiller, S., Soltanieh, S., Server, K.L., Mak, R., Jin, W., Fang, M.Y., Luo, E.C., Krach, F., Yang, D., Sen, A., et al. (2018). Context-Dependent and Disease-Specific Diversity in Protein Interactions within Stress Granules. Cell *172*, 590–604.e13. https://doi.org/10.1016/j.cell.2017.12.032.
82. Begovich, K., Vu, A.Q., Yeo, G., and Wilhelm, J.E. (2020). Conserved metabolite regulation of stress granule assembly via AdoMet. J. Cell Biol. *219*, e201904141. https://doi.org/10.1083/jcb.201904141.
83. Raices, M., and D'Angelo, M.A. (2022). Analysis of Nuclear Pore Complex Permeability in Mammalian Cells and Isolated Nuclei Using Fluorescent Dextrans. Methods Mol. Biol. *2502*, 69–80. https://doi.org/10.1007/978-1-0716-2337-4_4.
84. Rappsilber, J., Mann, M., and Ishihama, Y. (2007). Protocol for micro-purification, enrichment, pre-fractionation and storage of peptides for proteomics using StageTips. Nat. Protoc. *2*, 1896–1906. https://doi.org/10.1038/nprot.2007.261.
85. Van Nostrand, E.L., Nguyen, T.B., Gelboin-Burkhart, C., Wang, R., Blue, S.M., Pratt, G.A., Louie, A.L., and Yeo, G.W. (2017). Robust, Cost-Effective Profiling of RNA Binding Protein Targets with Single-end Enhanced Crosslinking and Immunoprecipitation (seCLIP). Methods Mol. Biol. *1648*, 177–200. https://doi.org/10.1007/978-1-4939-7204-3_14.
86. Love, M.I., Huber, W., and Anders, S. (2014). Moderated estimation of fold change and dispersion for RNA-seq data with DESeq2. Genome Biol. *15*, 550. https://doi.org/10.1186/s13059-014-0550-8.

Please cite this article in press as: Al-Azzam et al., Inhibition of RNA splicing triggers CHMP7 nuclear entry, impacting TDP-43 function and leading to the onset of ALS cellular phenotypes, Neuron (2024), https://doi.org/10.1016/j.neuron.2024.10.007

STAR★METHODS

KEY RESOURCES TABLE

REAGENT or RESOURCE	SOURCE	IDENTIFIER
Antibodies		
Mouse anti-CHMP7	Proteintech	cat# sc-271805; RRID: AB_10707824
Rabbit anti-CHMP7	Abcam	cat# 16424-1-AP; RRID: AB_2079500
Rabbit anti-CHMP7	Fortislife	cat# ab242221
Rabbit anti-CHMP7	Proteintech	cat# A305-734A; RRID: AB_2891637
Rabbit anti-TDP-43	Proteintech	cat# 10782-2-AP; RRID: AB_615042
Mouse anti-TDP-43	Invitrogen	cat# 60019-2-Ig; RRID: AB_2200520
Rabbit anti-DDX43	Invitrogen	cat# PA5-31486
Rabbit anti-TUBA1B	Proteintech	cat# PA5-112827; RRID: AB_2867561
Rabbit anti-SNRPD1	LSBio	cat# 10352-1-AP; RRID: AB_2193875
Rabbit anti-SNRPD1	Proteintech	cat# LS-C314704
Mouse anti-FAM120C	Invitrogen	cat# 25987-I-AP
Rabbit anti-DHX8	Proteintech	cat# PA5-61923; RRID: AB_2640596
Mouse anti-XPO7	Abcam	cat# 12980-I-AP
Mouse anti-Tubulin	Proteintech	cat# ab52866; RRID: AB_869989
Mouse anti-NOVA2	Abcam	cat# 55002-I-AP
Rabbit anti-MAP2	Cell Signaling	cat# ab5392; RRID: AB_2138153
Rabbit anti-GAPDH	Abcam	cat# mAb2118; RRID: AB_561053
Rabbit anti-POM121	Abcam	cat# ab254920
Rabbit anti-NUP414	Santa Cruz	cat# ab24609; RRID: AB_448181
Mouse anti-NUP133	Abcam	cat# sc-376699; RRID: AB_11149388
Rabbit anti-SMN/Gemin1	Abcam	cat# EPR25897-27
568 Goat Anti-Rabbit	Abcam	cat# ab175471; RRID: AB_2576207
488 Goat Anti-Mouse	Abcam	cat# ab150113; RRID: AB_2576208
647 Goat Anti-Rabbit	Abcam	cat# ab150083; RRID: AB_2714032
647 Goat Anti-Chicken	Abcam	cat# ab150175; RRID: AB_2732800
488 Goat Anti-Rabbit	Abcam	cat# ab150077; RRID: AB_2630356
555 Goat anti-Mouse	Invitrogen	cat# A28180; RRID: AB_2536164
647 Goat anti-Mouse	Invitrogen	cat# A32728; RRID: AB_2633277
488 Goat anti-Rabbit	Invitrogen	cat# A32731; RRID: AB_2633280
Anti-rabbit IgG	Cell Signaling	cat# 7074; RRID: AB_2099233
Anti-mouse IgG	Cell Signaling	cat# 7076; RRID: AB_330924
Biological samples		
Non-neurologic control, 50, F	Answer ALS Consortium	CS2AE8
Non-neurologic control, 58, F	Answer ALS Consortium	CS8PAA
Non-neurologic control, 78, F	Lothian Birth Cohort	EDi034-A
Non-neurologic control, 79, F	Lothian Birth Cohort	EDi036-A
Non-neurologic control, 51, M	CS iPSC Core Repository	CS0002
Non-neurologic control, 53, M	Track ALS	CS9XH7
Non-neurologic control, 79, M	Lothian Birth Cohort	EDi022-A
Non-neurologic control, 60, M	Answer ALS Consortium	CS1ATZ
C9orf72 HRE, 63, F	Answer ALS Consortium	CS0BUU
C9orf72 HRE, 52, F	Answer ALS Consortium	CS0NKC
ALS, 66, F	Answer ALS Consortium	CS0MBU

(*Continued on next page*)

Continued

REAGENT or RESOURCE	SOURCE	IDENTIFIER
ALS, 71, F	Answer ALS Consortium	CS0ZG5
ALS, 61, F	Answer ALS Consortium	CS2NDD
ALS, 45, F	Answer ALS Consortium	CS2WW0
ALS, 57, F	Answer ALS Consortium	CS3BYN
ALS, 60, F	Answer ALS Consortium	CS3EPR
C9orf72 HRE, 67, M	Answer ALS Consortium	CS0LPK
C9orf72 HRE, 52, M	Answer ALS Consortium	CS6CLW
ALS, 66, M	Answer ALS Consortium	CS2DXH
ALS, 62, M	Answer ALS Consortium	CS2VWR
ALS, 51, M	Answer ALS Consortium	CS0TBJ
ALS, 65, M	Answer ALS Consortium	CS0XXK
ALS, 67, M	Answer ALS Consortium	CS0YJY
ALS, 70, M	Answer ALS Consortium	CS1TBR
Chemicals, peptides, and recombinant proteins		
Y-27632 (ROCK inhibitor)	Tocris	cat# 1254
SB431542	Tocris	cat# 1614
CHIR99021	Tocris	cat# 4423
Dorsomorphin Dihydrochloride	Tocris	cat# 3093
GDNF	R&D syst	cat# 212-GD
CNTF	R&D syst	cat# 257-NT/CF
BDNF	R&D syst	cat# 248-BD
DAPT	Tocris	cat# 2634
SAG	Tocris	cat# 4366
Retinoic acid	Sigma-Aldrich	cat# R2625
SMN inhibitor	ProbeChem	cat# PC-49646
Matrigel	Corning	cat# 354230
Geltrex	ThermoFisher	cat# A1413302
Poly-D-Lysine	Sigma-Aldrich	cat# P6407-5mg
Laminin	ThermoFisher	cat# 23017-015
Laminin	Sigma-Aldrich	cat# L2020
mTeSR Plus 5X Supplement	STEMCELL Technologies	cat# 100-0275
mTESR Plus Basal Medium	STEMCELL Technologies	cat# 100-0274
DMEM/F12+Glutamax	ThermoFisher	cat# 31331028
Pen/Strep	ThermoFisher	cat# 15140122
N2 Supplement	Invitrogen	cat# 17502-048
B27 Supplement	Invitrogen	cat# 17504-044
Accutase	ThermoFisher	cat# A11105-01
FBS	ThermoFisher	cat# 10500-064
OptiMEM	ThermoFisher	cat# 51985026
Lenti-X™ Concentrator	Takarabi	cat# 631232
QuickExtract	Biosearchtech	cat# QE0905T
High-Fidelity DNA polymerase	NEB	cat# M0492L
Lipofectamine 3000 Transfection Reagent	ThermoFisher	cat# L3000001
Lipofectamine RNAiMax	Invitrogen	cat# 13778
Paraformaldehyde	Fishersci	cat# 15713
Triton-X	SigmaAldrich	cat# 9002-93-1
Goat serum	SigmaAldrich	cat# G9023
DAPI	Vectashield	cat# ZH1021
70 kDa Rhodamin-Dextran	Molecular Probes	N/A

(*Continued on next page*)

Please cite this article in press as: Al-Azzam et al., Inhibition of RNA splicing triggers CHMP7 nuclear entry, impacting TDP-43 function and leading to the onset of ALS cellular phenotypes, Neuron (2024), https://doi.org/10.1016/j.neuron.2024.10.007

Continued

REAGENT or RESOURCE	SOURCE	IDENTIFIER
Protease Inhibitor	SigmaAldrich	cat# P8340
Dynabeads Protein G	Invitrogen	cat# 01200616
Trypsin	Promega	cat# 487603
NP-40	Igepal	cat# CA630
RNase I	Ambion	cat# AM2294
RNA dephosphorylation with FastAP	ThermoFisher	cat# EF0651
T4 PNK	NEB	cat# M0201S
T4 RNA ligase 1	NEB	cat# M0204S
Superscript III	Invitrogen	cat# 12574026
Trizol reagent	Invitrogen	cat# 15596026
Critical commercial assays		
TruSeq stranded mRNA Library Preparation kit	Illumina	N/A
Direct-zol RNA Miniprep Kit	Zymo	cat# R2052
BCA assay	Pierce	cat# 23225
Colorimetric glutamate	Abcam	cat# Ab83389
Nuclei Pure Prep Nuclei Isolation Kit	Sigma-Aldrich	cat# NUC201-1KT
siRNAs On-TARGETplus SMARTpool	Dharmacon	N/A
Deposited data		
RAW files of bulk RNA seq and eCLIP	This paper	GEO: GSE25421
RAW files of proteomics data	This paper	MassIVE: MSV000093914
ENCODE3 eCLIP data	Van Nostrand et al.[43]	N/A
Experimental models: Cell lines		
sALS, 49, M	Krach et al.[48]	ukerizxx-E16
sALS, 49, M	Krach et al.[48]	ukerizxx-E10
sALS, 22, M	Krach et al.[48]	Ukeriu5q-SC-1
sALS, 22, M	Krach et al.[48]	Ukeriu5q-E-8
Non-neurologic control, 60, M	Gore et al.[71]	CV-B human
Non-neurologic control, 60, F	Cedars Sinai	CS6WMWiCTR-n2
Non-neurologic control, 20, F	Cedars Sinai	CS3JXYiCTR-n6
fALS C9ORF72 expansion (C9-10), 69, F	This paper	N/A
fALS C9ORF72 expansion (C9-12), 70, M	This paper	N/A
HEK293T	ATCC	cat# CRL-3216; RRID: CVCL_0063
HeLa	ATCC	cat# CCL-2; RRID: CVCL_0030
Oligonucleotides		
STMN2 Fwd	Integrated DNA Technologies	AGC TGT CCA TGC TGT CAC TG
STMN2 Rev	Integrated DNA Technologies	GGT GGC TTC AAG ATC AGC TC
Truncated STMN2 Fwd	Integrated DNA Technologies	GGA CTC GGC AGA AGA CCT TC
Truncated STMN2 Rev	Integrated DNA Technologies	GCA GGC TGT CTG TCT CTC TC
GAPDH	Integrated DNA Technologies	Hs.PT.39a.22214836
SNRPD1	GeneCopoeia, Inc.	HQP070792
NOVA2	Integrated DNA Technologies	Hs.PT.58.4896162
DHX8	Integrated DNA Technologies	Hs.PT.58.2034127
XPO7	Integrated DNA Technologies	Hs.PT.58.26574839
Recombinant DNA		
SNRPD1	GeneCopoeia, Inc.	NM_006938.3
CHMP7	Origene	NM_152272
TDP43 (TARDBP)	Origene	NM_007375
GFP-CHMP7-Helix5- Helix6 $^{NES1-\&NES2-}$	Gatta et al.[45]	N/A

(*Continued on next page*)

Please cite this article in press as: Al-Azzam et al., Inhibition of RNA splicing triggers CHMP7 nuclear entry, impacting TDP-43 function and leading to the onset of ALS cellular phenotypes, Neuron (2024), https://doi.org/10.1016/j.neuron.2024.10.007

Continued

REAGENT or RESOURCE	SOURCE	IDENTIFIER
GFP-CHMP7-Helix6 $^{NES2-}$	Gatta et al.[45]	N/A
Software and algorithms		
CRaft-ID	Wheeler et al.[23]	https://github.com/YeoLab/CRaftID
Skipper software	Boyle et al.[42]	data https://github.com/YeoLab/skipper.
Metadensity software	Her et al.[47]	https://github.com/YeoLab/Metadensity.
FastQC (Version 0.12.0)	Babraham Bioinformatics	https://www.bioinformatics.babraham.ac.uk/projects/fastqc/
STAR: ultrafast universal RNA-seq aligner	Dobin et al.[72]	N/A
FeatureCounts	Liao et al.[73]	N/A
Gorilla	Eden et al.[74]	N/A
rMATS (v4.1.2)	Shen et al.[75]	https://github.com/Xinglab/rmats-turbo
HydRA (v0.1.21.28)	Jin et al.[40]	https://github.com/Wenhao-Jin/HydRA
Metascape	Zhou et al.[76]	metascape.org
HOMER (v0.4.11)	Heinz et al.[77]	http://homer.ucsd.edu/homer/
Spectronaut v16.0	Bruderer et al.[78]	N/A
Graphpad Prism (Version 9)	Graphpad	https://www.graphpad.com/
SnapGene (Version 4.3.11)	Dotmatics	http://www.snapgene.com/
IGV	Robinson et al.[79]	https://igv.org/doc/desktop/
Fiji	Schindelin et al.[80]	https://imagej.net/software/fiji/
Other		
96-well plates	Greiner Bio-One	cat# 07-000-166
6-well plates	ThermoFisher	cat# 89900
4%–12% BisTris gel	ThermoFisher	N/A
Zeiss LSM 880	Zeiss	N/A
Azure Biosystems c600 System	Azure Biosystems	N/A
CellRaft AIR® System	Cell microsystems	N/A
NovaSeq6000	Illumina	N/A

EXPERIMENTAL MODEL AND STUDY PARTICIPANT DETAILS

Induced pluripotent stem cells, differentiated motoneurons, and cell lines

In this study, we reprogrammed fibroblasts from two fALS patients, referred to as fALS (C9-10) and fALS (C9-12). The sALS lines used were obtained from a previous study.[48] Additionally, we used the CV-B iPSC line, which originates from Craig Venter and is publicly available, as previously described.[71] All other non-neurologic control lines were obtained from Cedars Sinai. All required material transfer agreements were filed and approved. Demographic information, including sex and age, for all cell lines is provided, and all lines are from individuals identified as White and non-Hispanic or Latino, as detailed in the key resources table.

Human motor neurons were differentiated from iPSCs as previously described.[81,82] iPSCs, before differentiation, were passaged with Accutase (StemCell Technologies: catalog #. At-104) and grown as a monolayer on feeder-free plates in mTeSR1(Lot #: 1000086203) and mTeSR Plus 5x supplement (StemCell Technologies: 100-0276). IPSCs were then plated on a Matrigel (Corning:354277). Once the cells reached >90% confluence, the medium was changed daily with N2B27 medium (DMEM/F12 + GlutaMAX (Life Technologies:10565018), 1% N-2 supplement(Invitrogen:17502048), 2% B-27 supplement (Thermo Fisher Scientific:17504044), 100 μM ascorbic acid (Sigma-Aldrich:A4544), and 1% penicillin/streptomycin), and supplemented with 1 μM dorsomorphin dihydrochloride(Tocris:3093), 10 μM SB431542(Tocris:1614), 3 μM CHIR99021 (Tocris:4423), and 5 μM Rock Inhibitor (Tocris: 1254) until day 6. On Day 6, cells were split using Accutase (StemCell Technologies:07921), and 3 million cells were plated on a 10 cm plate. From day 6 to 15, cells were fed daily with N2B27 medium supplemented with 1 μM dorsomorphin dihydrochloride (Tocris:3093), 10 μM SB431542 (Tocris:1614), 200 nM smoothened agonist (SAG; Milipore sigma: 566660), 1.5 μM retinoic acid (RA; Sigma-Aldrich:R2625), and 5uM Rock Inhibitor. On day 15, cells reached the motor progenitor stage and are dissociated using accutase and transferred to be plated on matrigel coated plates. The dissociated cells were seeded in N2B27 medium supplemented with 200 nM smoothened agonist (SAG; Tocris), 1.5 μM retinoic acid (RA; Sigma-Aldrich), and 10uM Rock Inhibitor, 20 ng/ml recombinant human brain-derived neurotrophic factor (BDNF, R&D syst:248-BD), 2 ng/ml recombinant human glial cell line–derived neurotrophic factor (GDNF.R&D syst:212-GD), and 2 ng/ml recombinant human ciliary neurotrophic factor (CNTF, R&D syst:257-NT/CF).

Two days post differentiation, neurons were grown with N2B27 medium, growth factor, 200nM SAG, 1.5 μM Retinoic acid, and 2 μM Rock Inhibitor. On day 19 to day 20, medium was modified with the addition of 2 μM N-[N-(3,5-difluorophenacetyl-l-alanyl)]-S-phenylglycine t-butyl ester (DAPT; Tocris:2634). Six days post differentiation (day 21), the medium was modified with a 5 μM rock inhibitor and kept with the same media until Day 28 when cells are fully mature.

Human HEK293T and HeLa were cultured in DMEM (Gibco) with 10% FBS (ThermoFisher).

METHOD DETAILS

Generating GFP-CHMP7 fluorescently labeled HeLa cells

The CHMP7 plasmid (NM_152272) was obtained from OriGene. The CHMP7 sequence was cloned into the pLenti-EF1a-SPdCas9-EGFP-2A-Blast vector (Addgene, Plasmid #52962) using Gibson assembly. HEK293T cells (70% confluent in a 10 cm dish) were transfected with the GFP-CHMP7 construct using Lipofectamine™ 3000 (ThermoFisher, L3000001). Media was harvested from HEK293T cells at 24 and 48 h post-transfection, and virus particles were concentrated using Lenti-X™ Concentrator (Takara, 631232) at a ratio of 1:3 volumes, overnight at 4°C. The resulting GFP-CHMP7 viral particles were used to infect HeLa cells. After 48 h, infected HeLa cells were selected with blasticidin and sorted by fluorescence-activated cell sorting (FACS).

Viral infection of HeLa cells with CRISPR-Cas9 library

CHMP7-GFP HeLa cells (5×10^6) were seeded onto four 10 cm plates. The following day, each plate received 13 μL of lentiviral particles in medium containing 8 μg/mL polybrene. After 24 h, the virus-containing medium was removed, and the transduced cells were treated with 2 μg/mL puromycin for 3 days. Cells from all plates were combined and seeded onto microRaft arrays for further analysis.

Preparation of CRISPR library virus

HEK293T cells were seeded at 60% confluency in six 15 cm plates the day before transfection. Transfection was performed using 100 μL Lipofectamine 3000, 85.8 μL P3000 reagent, 22.5 μg lentiCRISPR plasmid library, 15.9 μg pMD.2g, and 21.5 μg psPAX2. The medium was replaced with fresh DMEM supplemented with 10% FBS 24 h post-transfection. After 48 h, the supernatant was filtered through a 0.45 μm low protein-binding membrane and ultracentrifuged at 24,000 rpm for 10 min at 4°C. The viral pellet was resuspended in PBS overnight at 4°C and stored at −80°C.

Determination of multiplicity of infection (MOI)

To calculate the MOI, lentiviral titration was performed by transducing HeLa cells (7×10^5 cells/well in a 6-well plate) with varying volumes of virus (0.5–20 μL) in medium supplemented with 8 μg/mL polybrene for 24 h. The medium was then replaced (without polybrene), and half of the cells were split into replicate wells, one of which was treated with 2 μg/mL puromycin. After 3–4 days, cell numbers were counted, and the MOI was determined by identifying the viral volume that resulted in 15% cell survival.

MicroRaft cell culture

MicroRaft arrays were plasma-treated for 5 min (Harrick Plasma, Ithaca, NY) and sterilized by incubating in 75% ethanol for 30 min. After three consecutive 5-min rinses in 1× PBS, the arrays were coated with 0.001% w/v poly-D-lysine (PDL) for 1 h at 37°C, washed twice with 1× PBS, and stored in cell culture medium. A total of 1.2×10^4 cells (1:1 ratio of CHMP7-GFP and CRISPR-infected cells) were seeded onto each array in DMEM supplemented with 10% FBS and 1% Penicillin-Streptomycin (Gibco, 15140122). Arrays were centrifuged at 400 × g for 4 min to ensure even distribution of cells, then incubated at 37°C with 5% CO2. After 24 h, an additional 2 mL of medium was added to each microarray.

Guide identification of target wells

Isolated microRafts were stored at −20°C in QuickExtract buffer until library preparation. Genomic DNA was extracted following the manufacturer's protocol: 15 s vortex, incubation at 65°C for 6 min, 15 s vortex, and final incubation at 98°C for 2 min. PCR amplification was performed using Q5 High-Fidelity DNA Polymerase (NEB, M0492L). The first PCR round consisted of 22 cycles with primers targeting the regions flanking the CRISPR guides. Products from 4 individual reactions with unique indexing primers were pooled and purified using the Qiagen PCR purification kit. A second round of PCR was performed with 10 cycles using Illumina sequencing primers. Gel extraction was used to isolate the desired 260 bp product. Libraries were sequenced on an Illumina MiSeq platform. Detailed protocols for PCR and sequencing are available in Wheeler et al.[23]

siRNA transfections validation of candidates

For imaging in 96-well plates (GREINER BIO-ONE: 07-000-166), Hela pated $5.0X10^3$ were reverse transfected using 10 nM of siRNA (Dharmacon On-TARGETplus SMARTpool) and Lipofectamine RNAiMax (Invitrogen:13778), according to manufacturer's protocol, per well. After 72 h, cells were then fixed by adding 4% PFA to each well for 15 min at room temperature. Three washes with 1× PBS were performed to remove PFA. HeLa cells were immunostained for 1:20 mouse-monoclonal CHMP7 (sc-271805), Phalloidin-iFluor 488 Reagent (ab176753) and secondary antibody 1:1000 Goat Anti-Mouse IgG H&L (ab175473). Nuclei were stained with DAPI

(1:5000 v/v in PBS) for 30 min at room temperature. Cells were washed once with 1× PBS before being preserved in 50% v/v glycerol diluted in 1× PBS.

Immunofluorescence

To fix the cells (HeLa or Neuron), 12% paraformaldehyde (Fishersci:15713) was added to a final concentration of 4% PFA and incubated for 15 min at room temperature. Three washes with a wash buffer (0.01% Triton-X in 1× PBS) were performed to remove the PFA. Blocking and cell permeabilization were performed with 1-h incubation in 0.1% Triton-X (SigmaAldrich, 9002-93-1) and 5% goat serum (SigmaAldrich, G9023) diluted in 1× PBS. The cells were then washed with a wash buffer and incubated in the primary antibody solution overnight at 4°C (wash buffer with 5% goat serum). Samples were washed three times in wash buffer before being incubated in secondary antibody solution (wash buffer with 5% goat serum) Finally, cells were washed three times with 1x PBS and mounted with antifade mounting medium with DAPI (Vectashield, ZH1021).

Imaging

Zeiss LSM 880 confocal microscope was used to image all HeLa and iPSC-MNs. For super-resolution modalities or live cell experiments, 63x oil objective Airyscan was used for high-quality images acquired with very low laser power, 0.5%–1.0%, and without frame averaging, thus reducing phototoxicity.

Time-lapse imaging with SMN inhibitor

HeLa cells were transfected with CHMP7-GFP and TDP-43-mCherry and cultured for 24 h in a 35 mm glass dish. Before imaging, the cell culture medium was replaced with DMEM without phenol red. At time 0, after setting the imaging parameters, 200 μm of an SMN inhibitor (PC-49646) was added to the dish. Throughout the imaging process, cells were enclosed within an insulated chamber maintained at 37°C and 5% CO2. The GFP and RFP channels were captured every 10 min for 2 h, utilizing a 63X magnification, and Z-stacks consisting of 6–8 slices, separated by the recommended optimal distance. Image processing, including maximum Z-projections, was carried out using FIJI.

Dextran exclusion

Following a previously established protocol,[83] HeLa cells were treated with DMSO and 30 μm SMN inhibitor for 24 h. The detailed functional assay involved the inclusion of 0.2 mg/ml 70 kDa Rhodamin-Dextran (Molecular Probes) and 1 μg/ml DAPI.

Nuclear pore complex imaging

Nuclei were isolated from iPSC-MNs using the Nuclei Pure Prep Nuclei Isolation Kit (Sigma-Aldrich, NUC201-1KT) in accordance with the manufacturer's instructions. Following extraction, 10 to 50 μl of the obtained nuclei were then plated onto matri-gel-coated imaging chambers, and the subsequent immunofluorescence protocol mirrored the previously outlined procedure.

Glutamate toxicity

iPSCs were cultured in an iPSC growth medium following media protocol provided. To assess glutamate toxicity, at day 35 after SmD1 KD, iPSCs were either subject to 0 μM glutamate or 10 μM for 24 h. To provide glutamate levels and sensitivity a colorimetric glutamate assay kit (Abcam, Ab83389) was used.

Western blot

Cells were harvested from 6-well plates and pelleted by centrifugation in ice-cold PBS. Cell pellets were resuspended in 300 μL of RIPA buffer (ThermoFisher, 89900), supplemented with Protease Inhibitor (Sigma-Aldrich, P8340). Protein concentration was quantified using the BCA assay (Pierce, 23225). Equal amounts of protein (40 μg) were separated on 4%−12% Bis-Tris gels (ThermoFisher), and transferred to PVDF membranes. Membranes were blocked with 5% milk in TBST for 1 h at room temperature. Primary antibodies were used as described in the key resources table, including GAPDH (1:4000 in 5% milk in TBST) as a loading control, and incubated overnight at 4°C. Membranes were washed in TBST and incubated with HRP-conjugated secondary antibodies (Anti-rabbit IgG, HRP-linked, Cell Signaling, 7074; Anti-mouse IgG, HRP-linked, Cell Signaling, 7076), diluted 1:5000 in 5% milk in TBST for 2 h at room temperature. Detection was performed using Pierce™ ECL Western Blotting Substrate and SuperSignal™ West Femto Maximum Sensitivity Substrate on the Azure Biosystems c600 System.

Immunoprecipitations

Cell pellets were thawed on ice and lysed in 400 μl of lysis buffer (150 mM NaCl, 50 mM Tris pH 7.5, 1% IGPAL-CA-630, 5% Glycerol, and protease and phosphatase inhibitors), and split evenly (∼200 μl) into separate tubes. Half of the lysate was treated with 5 μl of 10 mg/ml RNase (Promega, 527491) and both lystates (+/- RNase) were incubated on ice for 20 min. Each tube was centrifuged at 4°C for 10 min at 14,000 g. The total protein concentration of each lysate was measured using a BCA assay to ensure that each sample had between 1-2 mg of total protein. 100 μl of Dynabeads Protein G (Invitrogen, 01200616) magnetic beads were washed 3 times in 1 ml lysis buffer and then conjugated to 10 μg of endogenous antibody (Fortislife, A305-734A). Bead-antibody conjugation was then added to the cell lysate and incubated overnight at 4°C on the rotator. The following day, samples were placed on a magnetic

bead separator, and the supernatant was removed. The samples were washed 2 times with a wash buffer (150 mM NaCl, 50 mM Tris pH 7.5, 5% Glycerol) containing 0.05% IGPAL and 2 times with a wash buffer without IGPAL. Beads were then incubated in 80 μl of on-bead buffer (2M urea, 50mM Tris (pH 7.5), 1 mM DTT, and 5 μg/mL Trypsin (Promega, 487603) for 1 h at 25°C on a shaker (1000 rpm). After 1 h, beads were placed on a magnetic bead separator and 80 μl of supernatant was transferred to a new tube. The beads were then washed twice with 60 μL of 2M urea and 50 mM Tris (pH 7.5) HPLC buffer. The supernatant from each wash was combined with the on-bead digest for a total of 200 μl per sample.

LC-MS/MS DIA

IP sample preparation

80ul of the partially digested proteins after trypsin digestion were used and disulfide bonds were reduced with 5 mM dithiothreitol (DTT) for 45 min at 600 rpm and 25°C. Cysteines were subsequently alkylated with 10 mM iodoacetamide (IAA) for 45 min in the dark at 600 rpm and 25°C. Samples were then further digested by adding 0.5 μg sequencing grade modified trypsin (Promega) for 16 h at 600 rpm and 25°C. After digestion, samples were acidified with a final concentration of 1% formic acid. Tryptic peptides were desalted on C18 StageTips according to Rappsilber et al.,[84] dried in a vacuum concentrator, and reconstituted in 15 μl of 3% acetonitrile/0.1% formic acid for LC-MS/MS.

MS/MS measurement

LC-MS/MS analysis was performed on a Q-Exactive HF. 5uL of total peptides were analyzed on a Waters M-Class UPLC using a 25cm Thermo EASY-Spray column (2um, 100A, 75um x 25cm) coupled to a benchtop ThermoFisher Scientific Orbitrap Q Exactive HF mass spectrometer. Peptides were separated at a flow rate of 400 nL/min with a 100 min gradient, including sample loading and column equilibration times. Data was acquired in data-independent mode. MS1 Spectra were measured with a resolution of 120,000, an AGC target of 5e6 and a mass range from 350 to 1650 m/z. 34 isolation windows of 38 m/z were measured at a resolution of 30,000, an AGC target of 3e6, normalized collision energies of 22.5, 25, 27.5, and a fixed first mass of 200 m/z.

IP MS analysis

Proteomics raw data was analyzed by Spectronaut v16.0 (Biognosys)[78] using a UniProt database (Homo sapiens, UP000005640), and MS/MS searches were performed under BGS factory settings with background imputation and automatic cross run normalization. Spectronaut Post Analysis software was used to calculate the average log2FC and unpaired Student's t test p values for CHMP7/IgG for RNase untreated and treated samples. 3 replicates of CHMP7 RNase untreated, CHMP7 RNase treated, IgG RNase untreated, and 2 replicates of IgG RNase treated were analyzed. High confidence interacting proteins were identified as those that were significantly enriched compared to RNase treatment matched IgG controls. Proteins with a FC > 2 and a p value < 0.01 (unpaired Student's t test) were determined to be enriched.

Enhanced crosslinking and immunoprecipitation (eCLIP)

Libraries were generated using standard eCLIP methods according to published protocols.[85] Motor neurons and Hela cells (2×10^7 for each replicate plate) were UV crosslinked (254 nm, 400 mJ/cm^2), then lysed and sonicated (Bioruptor) in eCLIP lysis buffer (50 mM Tris–HCl pH 7.4, 100 mM NaCl, 1% NP-40 (Igepal: CA630), 0.1% SDS, 0.5% sodium deoxycholate, 1:200 Protease Inhibitor Cocktail I, in RNase/DNase-free H_2O). RNA fragments were created by incubating lysates with RNase I (Ambion) and LUC7L2: RNA complexes were immunoprecipitated for 2 h at 4°C using Dynabeads bound to 4μg of LUC7L2-specific affinity-purified antibody. In parallel, libraries were generated from size-matched input (SMInput) samples containing RNAs present in the whole cell lysates, i.e. sans RBP-specific IP. For the IPs, a series of stringent washes (high salt wash buffer: 50 mM Tris–HCl pH 7.4, 1 M NaCl, 1 mM EDTA, 1% NP-40, 0.1% SDS, 0.5% sodium deoxycholate, in RNase/DNase-free H2O; wash buffer: 20 mM Tris–HCl pH 7.4, 10 mM MgCl2, 0.2% Tween-20, in RNase/DNase-free H2O) was followed by RNA dephosphorylation with FastAP (ThermoFisher) and T4 PNK (NEB) then ligation of an adaptor to the 3′ ends of the RNAs with T4 RNA ligase 1 (NEB). Protein:RNA complexes were separated on 4–12% polyacrylamide gels, transferred to a nitrocellulose membranes and RNA was extracted from the membranes using Proteinase K (NEB). Immunoprecipitation was confirmed by parallel western blotting of fractions of each sample with the antibody described previously. Following purification, SMInput RNA were dephosphorylated and 3′-ligated, and all samples were reverse transcribed with Superscript III (Invitrogen). Free primers were removed with ExoSap-IT (Affymetrix) and a DNA adaptor was ligated to the 3′ ends of the cDNA with T4 RNA ligase 1. cDNA was quantified by qPCR and PCR amplified using Q5 Master Mix (NEB) and resulting libraries were purified prior to Illumina sequencing.

RNA sequencing

Total RNA was extracted from HeLa cells using the Direct-zol RNA Miniprep Kit (Zymo, R2052). The integrity of the RNA (RNA integrity number; RIN) was evaluated using the Agilent 2100 Bioanalyzer. Subsequently, indexed cDNA libraries were generated with the TruSeq stranded mRNA Library Preparation kit from Illumina, and the sequencing was performed on a NovaSeq6000 (Illumina).

Gene expression profiling

After acquiring control and mutant sequences, reads were aligned using STAR: ultrafast universal RNA-seq aligner[72] to the reference GRCh38 annotation (GENCODE release 42). Once genes were aligned, reads aligned to genomic features were counted using featureCounts[73] and the same GRCh38 genome annotation file to quantify the number of reads per gene in the data. Differential expression analysis was done using DESeq2 v1.39.3[86] in R v4.1.3. The differentially expressed genes (DEGs) were further analyzed in Python to produce a volcano plot with a Benjamini-Hochberg adjusted p value cut-off of 0.05. Gene ontology analysis was completed using GOrilla.[74]

Alternative splicing analysis

The analysis of alternative splicing events between GFP-CHMP7^{NES2}- vs GFP-CHMP7 RNA-seq datasets was done using rMATS turbo v4.2.0. Five types of splicing events were calculated: alternative 3' splice-sites (A3SS), alternative 5' splice-sites (A5SS), skipped exons (SE), retained introns (RI) and mutually exclusive exons (MXE). The rMATS output comprises various metrics, with two primary ones being the False Discovery Rate (FDR) and the delta percent spliced in ($\Delta\Psi$). In our analysis, we first constructed a histogram to count alternative splicing events that met the following criteria: FDR ≤ 0.05 & $|\Delta\Psi| \geq 0.1$ (FDR + PSI) (Figure 5D). Using the genes found in the FDR + PSI subgroup as foreground and the remaining genes that had no significant AS events as background, we ran a Metascape analysis (Figure S4A).[76]

Alternative splicing events analysis for sALS and C9orf72 iPSC-MN vs Control iPSC-MN RNA-seq datasets was done using rMATS turbo v4.2.0. A 2x2 contingency table was constructed separating genes into 4 categories defined by combinations of significant vs insignificant AS genes and CHMP7 bounded vs not bounded genes. A Chi-squared statistic and the degrees of freedom were calculated and fed into scipy.stats.chi2's survival function to output a *p* value signifying a significant association between the significant alternatively spliced genes and CHMP7 bounded genes.

Quantification and statistical analysis for eCLIP data

Reads were processed using the Skipper processing pipeline, available at https://github.com/YeoLab/skipper [[https://doi.org/10.1101/2022.10.08.511447]]. In short, reads were trimmed of adapters with skewer [[https://doi.org/10.1186/1471-2105-15-182]], mapped with STAR (2.7.10a_alpha_220314) [[https://doi.org/10.1093/bioinformatics/bts635]] and PCR-deduped with UMIcollapse [[https://doi.org/10.7717/peerj.8275]]. Binding candidates were identified using a tiled window approach, where the 5' read ends (representing the crosslinking site) were counted across evenly sized windows for each genic region. Windows were then binned according to GC content to estimate and adjust for GC biases, and the comparison of IP reads to corresponding size-matched input (SMinput) reads were used to determine enrichment of signal above background.

qRT-PCR

Patient-derived sALS lines and IPSC-derived motor neurons were lysed with 300 μL of Trizol reagent (ThermoFisher), and RNA extraction was performed using Direct-zol RNA Miniprep Kit (Zymo Research, R2052). 1μg total of RNA was used for cDNA synthesis using the Applied Biosystems High-Capacity cDNA Reverse Transcription Kit (ThermoFisher, 2783736) and RNAse inhibitor Murine (New England Biolabs,10200656). For all qPCR reactions, individual master mixes for the primer sequences of interest were prepared in advance, each containing the primer itself, fluorescent monitor FastStart Universal SYBR Green Master ROX (Roche, 4913850001), and Nuclease Free H_2O. The primers used throughout the qPCR procedure were STMN2 (IDT), TRUNC STMN2 (IDT), GAPDH (IDT), and SNRPD1 (GeneCopoeia Inc.). STMN2 and Truncated STMN2 were used as targets to identify changes in stathmin length in the presence or absence of SNRPD1. GAPDH was used as a normalizing control, and SNRPD1 was used to evaluate the success of the initial knock down or overexpression from cell lines. Two representations of each sample were pipetted into a 384-well PCR plate.

QUANTIFICATION AND STATISTICAL ANALYSIS

In each experimental section described above, we conducted all data analysis using Fiji. The analysis process was either fully automated or conducted in a blinded manner. For statistical analyses, we utilized GraphPad Prism. In imaging experiments where we quantified multiple cells per iPSC line, we performed statistical analyses by considering the average number of cells evaluated per iPSC line, with the total sample size indicated in the figure legends. We employed the Student's t test as specified in the figure legends to assess statistical significance, with the following significance levels: $^{*}p < 0.05$, $^{**}p < 0.01$, $^{**}p < 0.001$, and $^{****}p < 0.0001$. To effectively visualize the complete distribution and variability of large datasets, we used violin plots. Note that the first violin plot dots are not presented due to the large dataset size (>500 cells analyzed).